

Quantifying numerical mixing in a tidally forced global eddy-permitting ocean model

Alex Megann*

National Oceanography Centre, Empress Dock, Southampton SO14 3ZH, UK

ARTICLE INFO

Keywords:

Global ocean model
Tides
Internal tides
Numerical mixing

ABSTRACT

An ensemble of experiments based on a $1/4^\circ$ global NEMO configuration is presented, including tidally forced and non-tidal simulations, and using both the default z^* geopotential vertical coordinate and the $z\sim$ filtered Arbitrary Lagrangian-Eulerian coordinate, the latter being known to reduce numerical mixing. This is used to investigate the sensitivity of numerical mixing, and the resulting model drifts and biases, to both tidal forcing and the choice of vertical coordinate. The model is found to simulate an acceptably realistic external tide, and the first-mode internal tide has a spatial distribution consistent with estimates from observations and high-resolution tidal models, with vertical velocities in the internal tide of over 50 metres per day. Tidal forcing with the z^* coordinate increases numerical mixing in the upper ocean between 30°S and 30°N where strong internal tides occur, while the $z\sim$ coordinate substantially reduces numerical mixing and biases in tidal simulations to levels below those in the z^* non-tidal control. The implications for the next generation of climate models are discussed.

1. Introduction

Substantial advances have been made over the last two decades in simulating tides in OGCMs with realistic domains and surface forcing (see [Arbic, 2022](#) for a comprehensive overview). [Arbic et al. \(2010\)](#) showed that a 0.08° global HYCOM model with realistic bathymetry and surface forcing represented the barotropic tide well, and that the internal tides were similar in both their spatial patterns and their amplitudes to those derived from satellite altimetry, even though only low internal modes were present. Several studies have found that adding tidal forcing to models tends overall to increase the realism of the models. The presence of tidal motions appears to give particular benefit in polar regions, where interactions between tides and sea ice contribute processes absent from non-tidal simulations. [Holloway and Proshutinsky \(2007\)](#) compared tidally forced and non-tidal models of the Arctic Ocean, summarizing that tidal-induced mixing in the Arctic Ocean plays an important role in the global conveyor belt. [Luneva et al. \(2015\)](#) investigated the influence of tidal forcing in a $1/4^\circ$ model of the Arctic, finding that the tidal motions caused significantly increased (and more realistic) levels of mixing, in particular between the cold halocline layer and the warm Atlantic Water layer, which was associated with enhanced melting of sea ice. [Jourdain et al. \(2019\)](#) reached a similar conclusion from a regional simulation of the Amundsen Sea with and without tidal

forcing.

Improvements in fidelity resulting from the inclusion of tidal forcing in OGCMs have also been found outside ice-covered regions. [Song et al. \(2023\)](#) compared global implementations of the Finite-volume Sea ice–Ocean Model (FESOM2.1) with and without explicit tidal forcing, concluding that tides strengthened both the upper and lower cells of the global overturning circulation, as well as the Antarctic Circumpolar Current (ACC). [Katavouta et al. \(2022\)](#) reported a marked improvement in the representation of critical water masses in a regional $1/12^\circ$ model of the Indonesian Archipelago when tides were present. Mixing from the barotropic tide has been hypothesized to be critical for realistic distributions of biogeochemical tracers on shelves ([Sharples et al., 2007](#)), as well as over mid-ocean ridges ([Tuerena et al., 2019](#)).

The contribution of turbulent mixing from internal tides to the total mixing in the ocean is estimated to be about 30 % of the total dissipation ([Egbert and Ray, 2001](#)). It is the dominant mechanism by which Antarctic Bottom Water is mixed with the overlying deep waters ([Hogg et al., 1982](#); [Munk and Wunsch, 1998](#); [St Laurent and Garrett, 2002](#); [De Lavergne et al., 2016](#)), thereby providing a balance over the long term to the production of bottom waters around Antarctica. Mixing from internal tides is also believed to be significant elsewhere, including playing a major role in supporting the meridional overturning circulation, which has been confirmed in numerical models ([Bryan, 1987](#); [Webb and](#)

* Corresponding author.

E-mail address: apm@noc.ac.uk.

<https://doi.org/10.1016/j.ocemod.2024.102329>

Received 20 September 2023; Received in revised form 16 January 2024; Accepted 17 January 2024

Available online 18 January 2024

1463-5003/© 2024 The Author(s). Published by Elsevier Ltd. This is an open access article under the CC BY license (<http://creativecommons.org/licenses/by/4.0/>).

Suginohara, 2001; Wunsch and Ferrari, 2004) and in laboratory experiments (Whitehead and Wang, 2008). Nevertheless, few global ocean models, particularly those with the horizontal resolution of between 0.25° and 1° that is currently typical of climate models, have historically included tidal forcing. The main reason for this is that such models either fail to represent the internal tide at all, or can resolve at most the first internal mode: the wavelength of a mode-1 internal tide with period 12 h is between 50 and 90 km, and that of the second mode typically between 40 and 55 km (e.g. Zhao, 2018). This means that these models are far from being able to simulate the energy cascade of internal waves down to wavelengths of a few hundred metres and high vertical modes (Garrett and Munk, 1975; Sakai et al., 2021), at which point they break and mixing occurs (Vic et al., 2019). As a result, internal tidal motions in these models cannot contribute significant levels of mixing through this mechanism.

Since models with eddy-permitting resolution are unable to represent the full internal tide spectrum, and hence omit the significant levels of mixing from this source, the mixing effect of tides is often provided by a parameterisation scheme. Following the pioneering work of St Laurent et al. (2002), practical implementations include those of Simmons et al. (2004), Jayne (2009), Saenko and Merryfield (2005) and of de Lavergne et al. (2020). Such schemes typically augment the vertical global mixing based on the large-scale stratification with locally enhanced mixing, based on the effect of rough bottom topography on stratified tidal flows that are derived from an external barotropic tidal model. The earlier approaches evaluate a spatially varying energy dissipation rate, according to local turbulent energy levels derived from the tidal velocity field, while that of de Lavergne et al. (2020) adds a representation of the effects of remotely generated internal tides.

A known weakness of models based on geopotential vertical coordinates is that the large vertical velocities that characterize internal waves and tides, which can exceed 50 m per day, cause vertical advection of tracers, and most numerical advection schemes have a small irreversible, or diffusive, component (Griffies et al., 2000), which leads to unphysical numerical tracer mixing. The default vertical coordinate in version 4 of the Nucleus for European Marine modelling of the Ocean (NEMO v4.0, Madec et al., 2019) is the nonlinear free surface or Variable Volume Layer (VVL) scheme (Adcroft and Campin, 2004; Levier et al., 2007), usually referred to in shorthand as z^* , which represents external gravity waves as changes to the layer vertical scale, scaled uniformly over the water column with the surface height anomaly. The z^* coordinate, of course, is not strictly speaking a “fixed” coordinate, since there is a relatively small vertical motion corresponding to the barotropic mode, but the latter does not correspond to any advective vertical velocity relative to the coordinate surfaces, and hence does not cause numerical mixing. Megann (2018) evaluated an effective diapycnal diffusivity based on density transformation in a global $1/4^\circ$ NEMO and found that over much of the ocean interior this was between five and ten times as large as the diffusivity calculated in the TKE mixing scheme of the model. The $z\sim$ vertical coordinate (Leclair and Madec, 2011) is intended to reduce this contribution to numerical mixing by replacing vertical velocities relative to a fixed grid from tides and internal gravity waves by displacements of the grid on timescales shorter than a few days, reverting to the z^* grid on longer timescales. Megann et al. (2022), henceforth referred to as MCS2022, used an ensemble of global $1/4^\circ$ NEMO simulations with z^* and $z\sim$ with a range of timescale parameters to demonstrate that $z\sim$ performs as intended, transforming advective vertical velocities, relative to the fixed vertical coordinate, associated with internal waves into near-adiabatic displacements of the vertical coordinate. In this configuration $z\sim$ was shown to give almost unequivocal improvements to model performance, reducing a diagnosed effective diapycnal diffusivity by at least 10 % and consistently reducing drifts in the temperature and salinity at all depths. Lengthening the filter timescale parameter from the default of 5 days up to 40 days was found to robustly strengthen the benefits of $z\sim$, after which point diminishing returns started to set in. A $z\sim$ coordinate has also been tested in idealised

domains using the Model for Prediction Across Scales-Ocean (MPA-S-Ocean; Petersen et al., 2015) and in version 6 of the Modular Ocean Model (MOM6, Adcroft et al., 2019). Using the latter model, Gibson et al. (2017) demonstrated that a $z\sim$ vertical coordinate unambiguously reduced numerical mixing from both horizontal and vertical advection. Until now, the effectiveness of the $z\sim$ coordinate has not been assessed in a realistic simulation with tidal forcing, but since the 12-hour and 24-hour periods of tidal forcing are well within the time scales addressed by $z\sim$, we expect it to confer similar advantages as those already demonstrated in the presence of internal waves.

In this paper we use the existing GO8p0 configuration as described in MCS2022, and extend the ensemble developed under that study to include tidal forcing. The main focus of the paper is on investigating the effect of the resolved low-mode internal tide on numerical mixing, and the effectiveness of the $z\sim$ vertical coordinate in reducing the numerical mixing from the vertical velocities associated with the internal tide. Since the model is far from being able to resolve the physical mixing from tides, the main aim in this instance is not to create an optimum tidally forced $1/4^\circ$ ocean simulation, and so relatively low priority is put on achieving realistic amplitudes of the five external tidal harmonics. We shall demonstrate that the model simulations nevertheless have an acceptably realistic external tide, and crucially that they have a representation of at least the first mode internal tide in each of the harmonic constituents that is realistic in its spatial structure and with a large enough amplitude in its vertical velocity to test the $z\sim$ scheme.

The questions we shall address in this paper are:

- (1) How well does the model simulate external and internal tides with z^* and $z\sim$, taking the limited resolution into account?
- (2) Does the $z\sim$ vertical coordinate work as designed in a tidally forced global configuration?
- (3) What is the sensitivity of numerical mixing to tidal forcing?
- (4) How much does $z\sim$ reduce numerical mixing from internal waves and tides?
- (5) How do tides and $z\sim$ affect model drifts and biases?

In Section 2 we describe the model and introduce the experimental design. In Section 3 we assess the representation of the external and internal tides in the simulations and perform first-order checks on the functioning of $z\sim$ in a model configuration with tidal forcing. In Section 4 we quantify the mixing in the simulations, and in Section 5 we investigate the effect of tides and $z\sim$ separately and in combination on the model fields and large-scale circulation. Finally, Section 6 is a Summary and Discussion.

2. Model description and experimental design

2.1. Model description

The GO8p0 model configuration used in this study is identical to that described in MCS2022, so we will include only a brief description here. It is based on the GO6/GO7 ocean configurations (Storkey et al., 2018), but is built on version 4.0 of the Nucleus for European Marine Modelling ocean model (NEMO v4.0, Madec et al., 2019), whose default sea ice component is the Sea Ice modelling Integrated Initiative model (SI³), whereas the earlier configurations used version 3.6-stable of NEMO and the CICE sea ice model. The grid is the eORCA025 extended global $1/4^\circ$ resolution grid (Barnier et al., 2006), which is a quasi-isotropic bipolar grid with poles at land points in Siberia and Canada, a southward grid extension to allow simulation of the Antarctic ice shelves (although the latter are not included in the present configuration), and a Mercator projection grid elsewhere. We note that the Arctic regional model used by Luneva et al. (2015) is an exact subdomain of the grid used in the present model, although those authors used a hybrid terrain-following vertical coordinate, in contrast to the fixed z^* vertical coordinate used here.

Horizontal viscosity is bilaplacian with the default value of $A_{Lm} = -1.5 \times 10^{11} \text{ m}^4 \text{ s}^{-1}$ at the Equator, with values reduced polewards as the cube of the maximum grid cell dimension to avoid instability in the momentum diffusion equation (see Griffies and Hallberg, 2000). Tracer advection is second-order Flux Corrected Transport (FCT), also known as Total Variance Dissipation (TVD; Zalesak, 1979), for both horizontal and vertical advection of tracers. Lateral diffusion of tracers is along isoneutral surfaces, with a coefficient of $150 \text{ m}^2 \text{ s}^{-1}$; the default in NEMO v4 is the scheme of Redi (1982), as implemented by Cox (1987). A mesoscale eddy parameterisation scheme is not used. The vertical mixing scheme is a modified version of the Turbulent Kinetic Energy (TKE) scheme (Gaspar et al., 1990; Madec et al., 2019), with a background vertical eddy diffusivity of $1.2 \times 10^{-5} \text{ m}^2 \text{ s}^{-1}$, which decreases linearly with latitude from 15°N and 15°S towards a value of $1.2 \times 10^{-6} \text{ m}^2 \text{ s}^{-1}$ between 5°N and 5°S .

The ocean is initialized at rest from a 1995–2004 average of the EN4 climatology (Good et al., 2013), and integrated from 1976 to 2005, forced with CORE2 interannual fields (Large and Yeager, 2009), with the last ten years used for the principal analysis. The forcing frequencies were as follows: 6-hourly wind speed, air temperature and humidity; daily longwave and shortwave radiation, with a diurnal cycle applied to the latter; and monthly mean precipitation.

2.2. The $z\sim$ vertical coordinate

Three of the experiments described here use the default z^* vertical coordinate, which, as noted in the Introduction, has been shown to produce spurious diapycnal mixing of tracers in the presence of internal waves, and we shall also present results from experiments with the $z\sim$ vertical coordinate. The implementation of this in NEMO v4.0 is identical to that described in MCS2022; Appendix A1 of that paper includes a full description of the operation of $z\sim$ as presented by Leclair and Madec (2011), and Appendix A2 describes the modifications applied to the code that are needed to ensure stable operation in a global domain with realistic bathymetry and coastlines. These include checks on negative thicknesses; strong restoration to z^* near the sea bottom; reversion to z^* in water shallower than 100 m; and extra thickness smoothing.

The $z\sim$ scheme in NEMO includes two timescale parameters: t_{\sim} is the filter timescale for frequency division between the quasi-isopycnal regime at high frequencies and the z^* regime at low frequencies, and t_z is the timescale for restoration of the interface depths to z^* . We select two pairs of values for these from the $z\sim$ ensemble described by MCS2022: the default settings of $t_{\sim}=5$ days and $t_z = 30$ days; and $t_{\sim}=20$ days and $t_z = 60$ days, the latter combination being found to give a marked enhancement, with respect to the default settings, of the effectiveness of $z\sim$ in reducing numerical mixing from internal waves at close to the inertial period.

2.3. Tidal forcing

Tidal forcing is applied in NEMO as an additional barotropic force in the momentum equation (see Madec et al., 2019 for details) and in the present application includes five tidal harmonics: the semidiurnal components M2, S2 and N2; and the diurnal components K1 and O1. The scalar approximation for self-attraction and loading (Accad and Pekeris, 1978), was applied. Log-layer bottom drag was enabled, with a base drag coefficient of 1.0×10^{-3} . It was found that tidal forcing with the standard eORCA025 bathymetry, using a default minimum depth of 9.8 metres (level 8), gave fatal errors at runtime, with unacceptably high velocities, so this was increased to 16.5 metres (level 11) for the tidally forced configurations.

Because the internal tide was not expected to be well resolved at the $1/4^\circ$ resolution, and was therefore unlikely to provide realistic levels of tidal mixing, a code modification was used (see Appendix A for details of the model sources) that applies the tidal mixing parameterisation of

Simmons et al. (2004), with modifications in the Indonesian through-flow region (Koch-Larrouy et al., 2008), to all the non-tidal experiments and all except one of the tidally forced experiments. We shall show that this scheme enhances the explicit diffusivity in the mixing scheme in the ocean interior over major bathymetric features.

2.4. Experimental design

The main aims of this study are twofold: firstly, to investigate the effects of tidal forcing on numerical mixing in a $1/4^\circ$ global NEMO configuration; and secondly, to evaluate the benefits of the $z\sim$ vertical coordinate in ameliorating the numerical mixing from the internal tide. To this end, we implement a six-member “main” ensemble consisting of three pairs of experiments, one of each pair tidally forced and the other not tidally forced; the first pair uses the z^* vertical coordinate; the second uses $z\sim$ with the default timescale parameters of $t_{\sim}=5$ days and $t_z=30$ days; and the third pair uses $z\sim$ with the timescale parameters extended to $t_{\sim}=60$ days.

Two additional z^* simulations are included. One experiment *zstar_notide_16m* does not apply tidal forcing, but uses the modified bathymetry used for the tidally forced experiments (i.e. a deeper minimum shelf depth); this is added to isolate any potential sensitivities of the metrics to the changed minimum shelf depth. The second, *zstar_tide_nomix*, has tidal forcing applied but the Simmons et al. (2004) tidal mixing parameterisation is not enabled; this serves to illustrate the limited ability of the existing TKE mixing scheme to represent the mixing effect of tides. Table 1 summarizes the experiments in the ensemble; we shall principally discuss the six “main” experiments, only adding the two additional experiments to line plots of global fields. We note that *zstar_notide*, *ztilde_5_notide* and *ztilde_20_notide* are the same simulations as those referred to as *zstar*, *ztilde_5_30* and *ztilde_20_60*, respectively, in MCS2022.

3. Assessment of the simulated external and internal tide

In this section we assess the external (barotropic) and internal (baroclinic) tides in the three main tidally forced simulations against both other general circulation models and high-resolution tidal models. Our objectives here are: to demonstrate firstly that the model is capable of simulating an acceptably realistic external tide; to show that internal tides are reproduced with realistic spatial distributions and with amplitudes that are sufficient to test the $z\sim$ coordinate; and finally that implementing $z\sim$ does not have a significant effect on the internal tide field.

3.1. Representation of the barotropic tide

The harmonics of the barotropic tide were evaluated for each integration from hourly sea surface elevation over the first three months of

Table 1
Model integrations.

Run	Vertical coord ^d	Z~ time scales	Tidal forcing	Tidal mixing param ⁿ	Min shelf depth
<i>zstar_notide</i>	z^*	-	N	Y	9.8 m
<i>ztilde_5_notide</i>	$z\sim$	5/30 days	N	Y	9.8 m
<i>ztilde_20_notide</i>	$z\sim$	20/60 days	N	Y	9.8 m
<i>zstar_tide</i>	z^*	-	Y	Y	16.5 m
<i>ztilde_5_tide</i>	$z\sim$	5/30 days	Y	Y	16.5 m
<i>ztilde_20_tide</i>	$z\sim$	20/60 days	Y	Y	16.5 m
<i>zstar_notide_16m</i>	z^*	-	N	Y	16.5 m
<i>zstar_tide_nomix</i>	z^*	-	Y	N	16.5 m

1996, and we validate them here against the respective harmonics from the FES2014 global ocean tide atlas (Lyard et al., 2021). Fig. 1 shows the amplitudes and phases for the FES2014 harmonics (left column) and those from the *zstar_tide* simulation (middle column), along with the differences between the amplitudes of the respective harmonic in the model with respect to the FES2014 dataset (right hand column), while Table 2 lists the RMS amplitudes of each harmonic in FES2014 and *zstar_tide*, with the global RMS error in each case of the model with respect to FES2014. The amplitude of the M2 semidiurnal tide in *zstar_tide* (Figs. 1(b)) is 10–30 % larger than in FES2014, while those of S2 and N2 (Figs. 1(e) and 1(h)) are a little smaller, although the locations of the largest tides in all the harmonics in the simulation are generally close to those in the reference, as are the amphidromes (locations of zero amplitude). The diurnal tides K1 and O1 (Figs. 1(k) and (e)) are comparable in both amplitude and phase to the reference.

It is of interest to compare the errors for the M2 barotropic tide shown in Fig. 1 and the top row of Table 2 to those presented by Pringle et al. (2021) and Barton et al. (2022) for tidal simulations on

Table 2

The RMS external tide amplitude in the FES2014 dataset; the RMS amplitude in *zstar_tide*; and global RMS errors of the *zstar_tide* simulation with respect to the respective harmonic of FES2014.

Harmonic	FES2014 RMS (m)	<i>zstar_tide</i> RMS (m)	RMS error (m)
M2	0.243	0.314	0.118
S2	0.097	0.147	0.043
N2	0.051	0.056	0.028
K1	0.095	0.107	0.035
O1	0.072	0.079	0.048

unstructured mesh grids. The RMSE of the M2 tide over the global domain in the present control simulation is 11.8 cm, which lies between the “deep” and “shallow” RMSE values in Table 3 of Pringle et al. (2021), but is larger than the global RMSE values listed in Fig. 8 of Barton et al. (2022) for most of the simulations described in that paper.

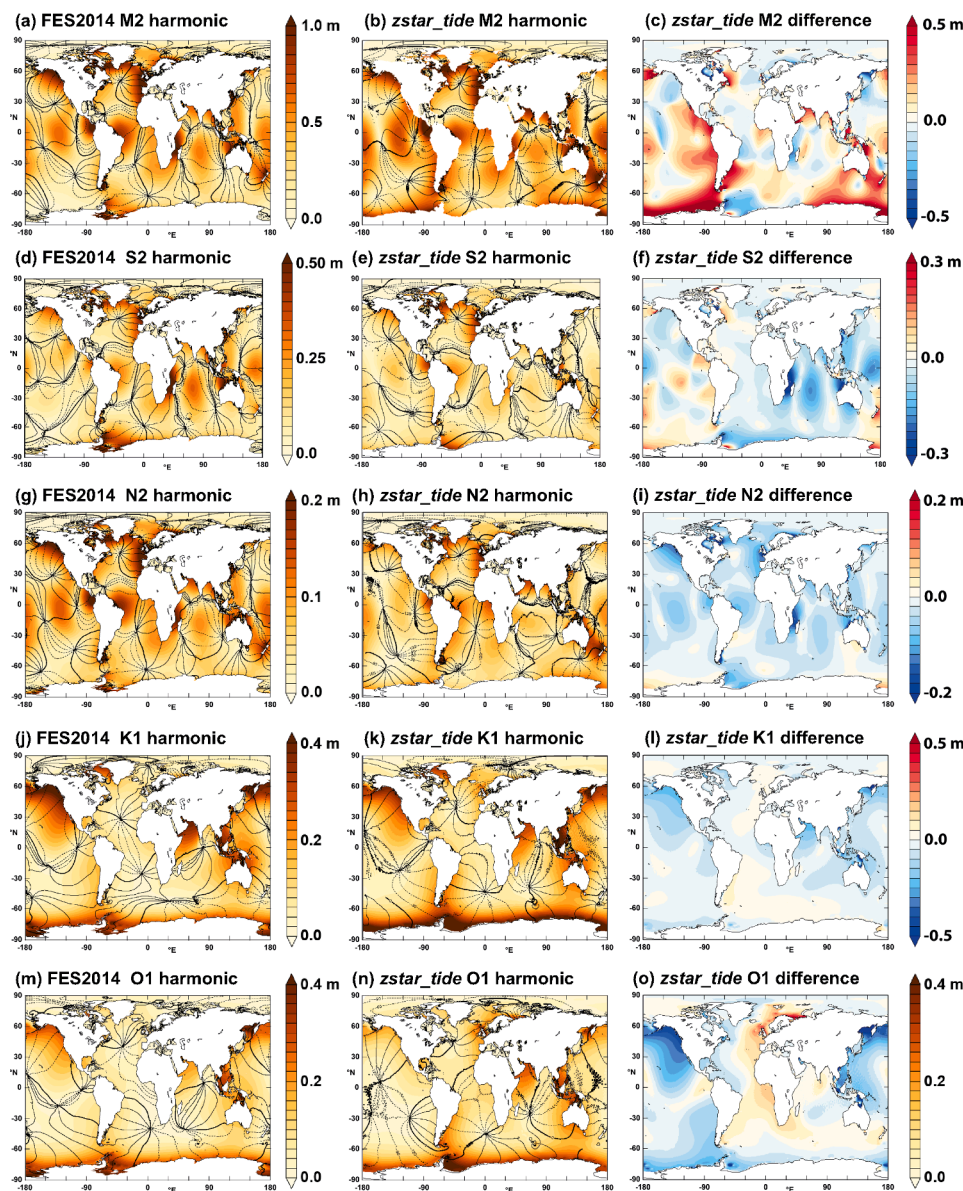


Fig. 1. Tidal harmonic amplitudes of surface elevation in metres: the left column shows amplitudes from the FES2014 dataset; the centre column shows those from the *zstar_tide* simulation; and the right column shows the differences in the amplitudes between FES2014 and *zstar_tide*. The black contours show the phase of each harmonic, with dashed lines representing a negative sign of the phase.

Table 3

The global RMS amplitude (in mm) of the surface elevation projection of each of the interior tide harmonics in the three tidally forced simulations, and the difference between the RMS amplitude between *ztilde_20_tide* and *zstar_tide*.

Harmonic	<i>zstar_tide</i> RMS (mm)	<i>ztilde_5_tide</i> RMS (mm)	<i>ztilde_20_tide</i> RMS (mm)	<i>ztilde_20_tide</i> minus <i>zstar_tide</i>
M2	5.445	5.440	5.449	0.004
S2	2.565	2.559	2.562	-0.003
N2	0.842	0.835	0.821	-0.021
K1	1.505	1.510	1.519	0.014
O1	1.166	1.174	1.175	0.009

3.2. Representation of the internal tide

With a fixed vertical coordinate, it is straightforward to discuss the internal tide in terms of the vertical velocity with respect to the fixed coordinate surface; we could also in principle validate this field against measurements of the vertical velocity from moored arrays. In the case of the z -coordinate, however, it is not appropriate to define the internal tide in terms of vertical velocities with respect to the model grid, so we use the method introduced by Ray and Mitchum (1997), which has been applied to satellite altimeter data by Ray and Zaron (2016), Zhao et al. (2016) and others, and to the simulated surface elevation in a global $1/12^\circ$ model by Arbic et al. (2012), to derive a representation of the internal tides that will enable us to characterize the sensitivity of the internal tide consistently for all the tidally forced experiments. This involves projecting the sea surface height onto each of the harmonic frequencies, and for each component applying a low-pass spatial filter to isolate the large-scale external component (the effect on the sea-surface height) of the internal tidal signal. The low-pass filtered signal is then subtracted from the original harmonic, and most of the residual signal in the surface height will therefore be associated with the internal tide. In this case we use a Hanning smoother with width 9 grid cells; this choice of parameter was chosen to separate the length scales of the internal and external tides, and little sensitivity was found to modest increases in the parameter.

Fig. 2 shows the surface signature of the M2 semidiurnal and the K1

diurnal internal tides, evaluated as above. The panels for M2 can be compared directly with Fig. 4(a) of Zhao et al. (2016), which shows the global M2 surface tide derived from satellite altimetry: the spatial structure of the regions of high amplitude in the simulations correspond well to those in the observational estimate, although the amplitude of the simulated internal tide is less than half that in the altimetry data in the Pacific, and still weaker in the Atlantic. We also compare Fig. 2(a–c) with Fig. 8 of Arbic (2022), which shows the M2 component of the SSH variability around the Hawaiian Archipelago in a range of tidal models along with the $1/12^\circ$ tidally forced simulation of the Hybrid Coordinate Ocean Model (HYCOM, Bleck, 2002): the amplitude of the M2 component in the present model is between 30 and 50 % of that in the $1/12^\circ$ simulation, but comparable with that in several of the other tidal models with a similar resolution to that of the present configuration. This reduction in internal tide energy in the present $1/4^\circ$ configuration is not altogether surprising, since the first baroclinic mode of the semidiurnal tide typically has a wavelength of between 50 and 90 km (e.g. Zhao, 2018), so is only marginally resolved in most locations at the $1/4^\circ$ resolution of the eORCA025 grid. Examination of the vertical structure of the vertical velocity in *zstar_tide* (see Fig. 4(d), for example) confirms that the internal tide in this configuration is present almost exclusively in the first baroclinic mode.

It is of note that the largest amplitudes of the internal tides – even of the semidiurnal components – are found mainly between 30°S and 30°N , and especially in the Pacific, where energetic sources of internal tides include the Izu-Ogasawara-Marianas Ridge south of Japan, the Solomon Archipelago east of Papua New Guinea, the Hawaiian Ridge, and the Tuamotu Archipelago south of the Equator.

The SSH projection of the internal tide is found to be only weakly sensitive to the choice of vertical coordinate. Table 3 lists the RMS value of the surface elevation projected onto the five tidal harmonics for each of the tidally forced simulations, along with the difference in global RMS signal between *ztilde_20_tide* and *zstar_tide*. The RMS value in *ztilde_20_tide* is not consistently larger or smaller than in *zstar_tide*, and the fractional differences with z - in the M2 and S2 semidiurnal tides are of order 10^{-3} , which we do not consider significant.

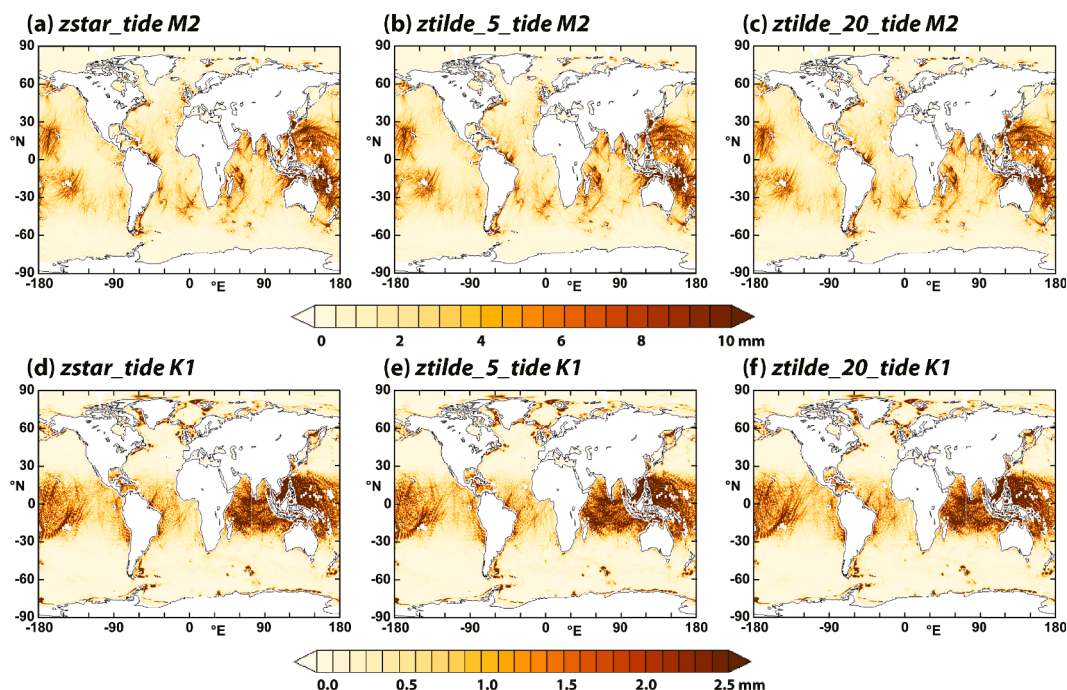


Fig. 2. The surface signature of the internal tide, calculated using the method of Arbic (2012): the M2 harmonic in (a) *zstar_tide*; (b) *ztilde_5_tide*; and (c) *ztilde_20_tide*; and that of the K1 internal tide in (d) *zstar_tide*; (e) *ztilde_5_tide*; and (f) *ztilde_20_tide*.

3.3. Transformation of Eulerian tidal velocities by the $z\sim$ coordinate

MCS2022 demonstrated the effectiveness of $z\sim$ in converting vertical velocities relative to the fixed z^* coordinate grid on timescales typical of internal waves into displacements of the grid. We shall, for the sake of consistency with the definition used by MCS2022, refer in shorthand to vertical velocities relative to the model grid as “Eulerian” vertical velocities, even in the case of $z\sim$ where the grid is not fixed in space. In fact, the velocities at grid points of the z^* coordinate are not rigorously Eulerian either, since the heights of the levels in that case are scaled by the barotropic surface elevation. Nevertheless, the present definition is useful as it refers to advective vertical velocities relative to the grid that have the potential to cause numerical mixing. Using as a case study a water column in the subtropical North Atlantic where energetic Near-Inertial Gravity Waves (NIGWs) occur, a reduction in the Eulerian vertical velocity, with respect to that in the z^* control, of a factor of 4 with the default $z\sim$ timescale parameters and a factor of 25 with the longest timescales was observed. Since the semidiurnal and diurnal tides have periods comparable to those of near-inertial gravity waves (the latter have periods between 15 and 24 h in the latitude range 30–50°N), we expect this coordinate to be equally effective, with a given selection of timescale parameters, in its response to internal tides as it is with NIGWs.

Fig. 3 shows the hourly Eulerian vertical velocity on level 55 (a nominal depth of 2021 m) in the Pacific at the start of year 1996 of each of the six main experiments. In the non-tidally forced experiments (top panels), the NIGWs, which in z^* (Fig. 3(a)) are characterized by near-plane wave fronts with vertical velocities of up to 50 metres per day, are almost entirely converted in the $z\sim$ experiments (Fig. 3(b) and (c)) to vertical coordinate displacements, particularly with the longer $z\sim$ timescale (Fig. 3(c)). Equatorial waves, which were identified in a related NEMO simulation at the same resolution (Blaker et al., 2021), are visible within 8–10° of the Equator; since these have periods of between 2 and 8 days, the Eulerian velocities associated with these are only partially transformed into coordinate displacements, relative to the NIGWs and internal tides, with a 5-day filter timescale (Fig. 3(b)), but are substantially reduced in the case of the 20-day filter timescale (Fig. 3(c)).

When tidal forcing is introduced with z^* , the internal tides can be seen to dominate the internal wave field over much of the Pacific (Fig. 3

(d)). Internal tide trains with amplitudes greater than 50 metres per day are found almost everywhere in the basin west of about 130°W, radiating from the shelf edges and island chains. The directions and relative intensities of the tidal rays in this panel may be matched to many of those in the surface signatures of the internal tides (Fig. 2(a)): particularly strong internal tide fields are visible in both figures in the regions west of 180°E and around the Hawaiian Archipelago. A prominent exception to this is the large amplitude of the vertical oscillations associated with internal tides generated close to the Aleutian Archipelago (see Fig. 3(d)), which do not have a strong surface signature in Fig. 2 (a). Enabling $z\sim$ with tidal forcing (Fig. 3(e) and (f)) has a comparable effect as in the non-tidal simulations, and the signature of the internal tides in the Eulerian vertical velocities, as with that of the NIGWs, is reduced by at least a factor of ten. Comparing the equatorial waves between the top and bottom rows of panels in Fig. 3 confirms that they are unaffected to first order by the presence of tides; this is to be expected, since, as shown by Blaker et al. (2021), these are to first order deterministic, being locally forced by the wind stress.

Fig. 4 shows the vertical structure of the internal waves and tides in the tropical Pacific: here we plot the hourly mean Eulerian vertical velocity at the start of 1996 on a section south of Hawaii at 167°W from the Equator to 30°N. For reference, the Hawaiian Archipelago lies between 18.5°N and 28°N. This signal includes both the internal waves and, in the tidal simulations, the internal tide; these contributions may be distinguished by the absence of the internal tide signal in the non-tidal simulations. It can be seen in Fig. 4(a) and (d) that the NIGWs and internal waves in this configuration manifest predominantly in the first baroclinic mode, with maximum amplitudes generally occurring at between 1000 m and 3000 m depth in both cases; the internal tides are characterized by significantly higher vertical velocities than the NIGWs, with maximum values on this section of about 30 m day⁻¹ from NIGWs (Fig. 4(a)) and more than 50 m day⁻¹ from tides (Fig. 4(d)). We also note that the large Eulerian vertical velocities associated with the internal tides span almost the whole depth of the ocean, and in particular have significant magnitudes at depths of 200–500 m, characteristic of the seasonal thermocline. Equatorial waves are again visible within 10° of the Equator in both experiments using the default $z\sim$ timescale parameters (Fig. 4(b) and 4(e)), and again they are more strongly transformed by $z\sim$ with the longer timescales (Fig. 4(c) and 4(f)).

To demonstrate more quantitatively the effect of $z\sim$ on the internal

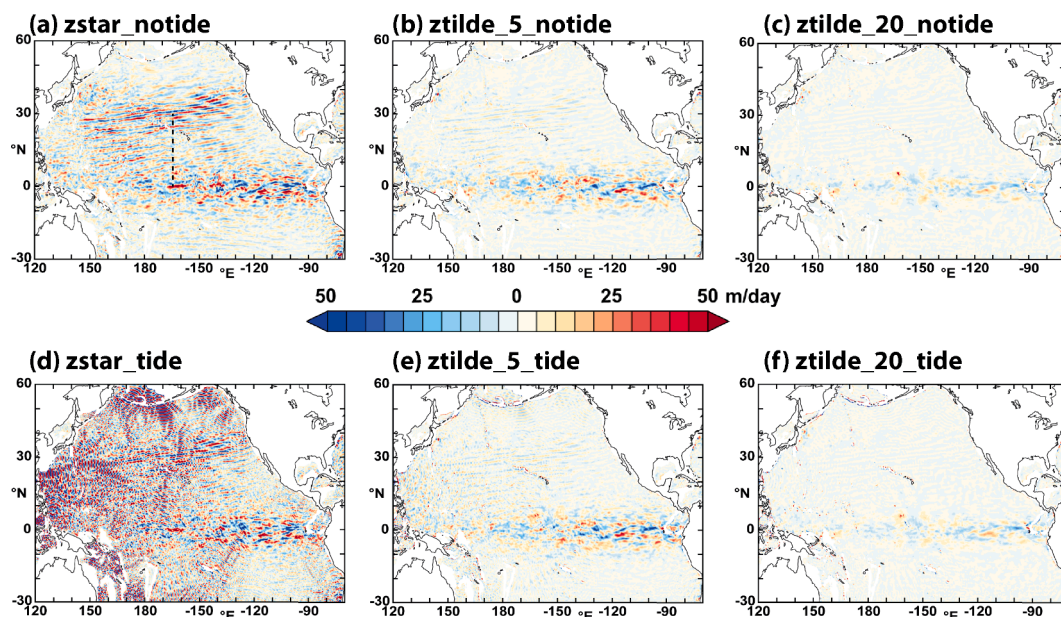


Fig. 3. Eulerian vertical velocities from a single hourly mean at the start of 1996 in the Pacific at nominal 2000 m depth in (a) *zstar_notide*; (b) *ztilde_5_notide*; (c) *ztilde_20_notide*; (d) *zstar_tide*; (e) *ztilde_5_tide*; and (f) *ztilde_20_tide*. The dashed black line in panel (a) indicates the position of the sections that will be plotted in Fig. 4.

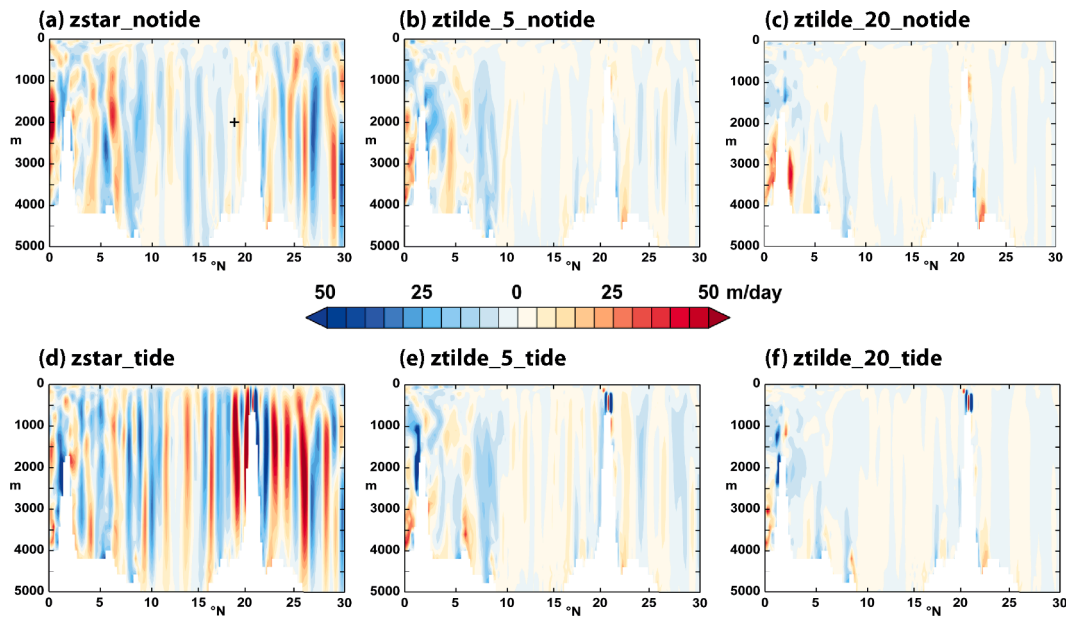


Fig. 4. Eulerian vertical velocity from a single hourly mean at the start of 1996 in the Pacific on a section at 167°W from the Equator to 30°N in (a) *zstar_notide*; (b) *ztilde_5_notide*; (c) *ztilde_20_notide*; (d) *zstar_tide*; (e) *ztilde_5_tide*; and (f) *ztilde_20_tide*. The “+” in Fig. 4(a) shows the position at 18°N, at which the time series displayed in Fig. 5 are evaluated.

waves and tides, we show in Fig. 5 ten-day time series of the hourly vertical velocity at the start of 1996 for each experiment at a point at 18°N, 167°W, south of the Hawaiian Archipelago (the location marked by a ‘+’ in Fig. 4(a)), where large internal tide amplitudes are observed. The black curves show the Eulerian vertical velocity on the level $k = 55$ with nominal depth 2022 m, and the red curves show the rate of change of height of the same depth coordinate level. As demonstrated by MCS2023 (albeit at a different location), the $z\sim$ coordinate successfully transforms most of the Eulerian, advective velocity associated with internal waves in the z^* case (panel (a)) to coordinate displacements (panels (b) and (c)), and in the case of the longest $z\sim$ timescales the Eulerian vertical motions are reduced by more than 90 %. Changing the vertical coordinate to $z\sim$ with tides again substantially reduces the Eulerian vertical velocity, and the amplitude of the residual vertical velocity signal in *ztilde_20_tide* (panel (f)) is reduced to a similar level as

that in the non-tidal experiment *ztilde_20_notide*. The rate of coordinate displacement in the $z\sim$ simulations is consistently in phase with the Eulerian vertical velocity with z^* , and with the timescale parameter set to 20 days has a very similar amplitude. The phase of the residual velocity (the black lines in Fig. 5(b), (c), (e) and (f)) in both tidal and non-tidal simulations, however, is delayed by approximately $\pi/2$, consistent with the action of a first-order filter, as noted by Leclair and Madec (2011). This means that there is an error in the phase of the advective vertical velocity, which may be resolved by using a higher order filter for $z\sim$ in future configurations.

In this section, we have confirmed that the model simulates a realistic external tide; that there is an acceptably realistic internal tide field, albeit almost exclusively in the first vertical mode and with an amplitude reduced to 30–50 % of that seen in observations and in higher resolution tidally forced models. We have demonstrated that the $z\sim$

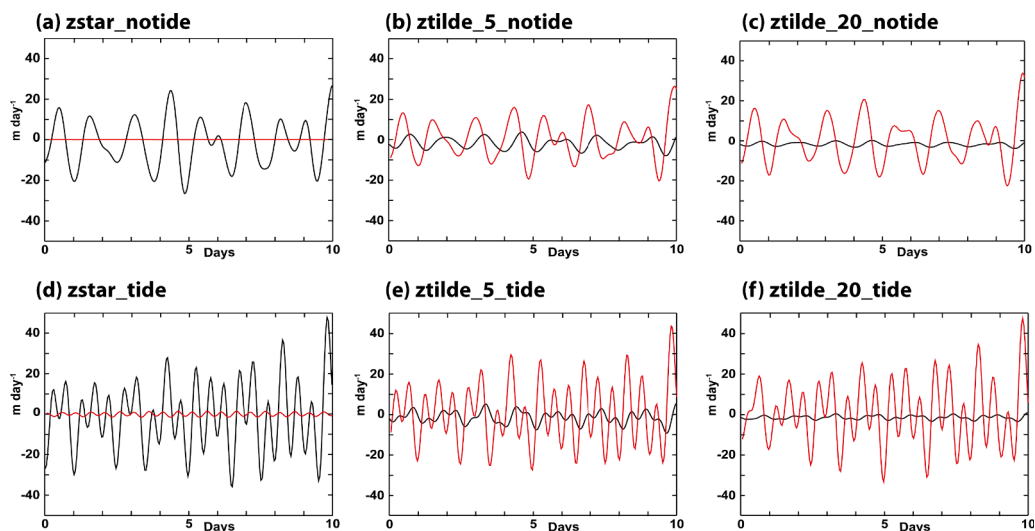


Fig. 5. Ten-day time series at the start of 1996 of the hourly mean Eulerian vertical velocity (black) and the rate of change of height (red) of the same depth coordinate level at a point south of the Hawaiian Archipelago at 18°N, 167°W on level $k = 55$ with nominal depth 2022 m in: (a) *zstar_notide*; (b) *ztilde_5_notide*; (c) *ztilde_20_notide*; (d) *zstar_tide*; (e) *ztilde_5_tide*; and (f) *ztilde_20_tide*.

coordinate functions as intended in reducing the advective Eulerian vertical velocity associated with numerical mixing by up to 90 % when there is a strong internal tide; and finally that $z\sim$ preserves the internal tide, both as represented by its signature in the surface elevation and also in terms of the transformation from its representation as vertical velocities in z^* simulations to coordinate displacements in simulations using $z\sim$.

4. Mixing analysis

4.1. Summary of analysis

The analysis, based on that of Lee et al. (2002), is identical to that described in Megann (2018) and again used by Megann and Storkey (2021) and in MCS2022. For clarity, we shall define again in this section the main quantities that we shall evaluate in Section 4.

A density transformation streamfunction $G(\Theta, \rho)$ is defined as

$$G(\Theta, \rho) = \Psi(\Theta, \rho) + \frac{\partial}{\partial t} V(\Theta, \rho) \quad (1)$$

where $\Psi(\Theta, \rho)$ is the overturning streamfunction at latitude Θ and potential density ρ , and $V(\Theta, \rho)$ is the volume below the isopycnal surface ρ and south of Θ . Considering only the ocean interior (defined as those regions in density space with potential density higher than the maximum monthly surface density over the 10-year analysis period), and assuming that the density transformation is entirely due to diffusive processes, we define a zonal mean effective diffusivity κ_{eff} as

$$\kappa_{\text{eff}}(\Theta, \rho) = \int_{\rho_{\text{max}}}^{\rho} \frac{\partial G(\Theta, \rho)}{\partial y} d\rho \bigg/ \int_{x_W}^{x_E} \frac{\partial \rho}{\partial z} dx \quad (2)$$

where x_W and x_E are the westward and eastward limits, respectively, of the basin at latitude Θ , and y is the northwards spatial dimension, with both x and y in metres. We note that Eqs. (1) and (2) neglect the contributions to the transformation rate from the nonlinearity of the equation of state, namely cabbeling and thermobaricity.

We evaluate κ_{eff} in the same set of potential density classes as used by Megann (2018) from 5-day means from the final ten years of the integrations (1996 to 2005). In the experiments with $z\sim$, the total effective meridional transport, including the ‘‘thickness diffusion’’ correction fluxes applied when the $z\sim$ coordinate is updated, is used for the calculation of the streamfunction in place of the simple advective flux. We note that ventilated density classes have been masked out in the calculation of global mean quantities in this paper, and as a result the appearance of some of the figures in this section differ from the corresponding figures in MCS2022.

Several approximations are made in deriving and evaluating Equation (2); these are discussed further in Appendix A, but we briefly summarise the most salient here.

1. The use of a zonally averaged stratification (the denominator of Eq. (2)) renders direct comparison between the effective diffusivity and the explicit diffusivity used in the model’s mixing scheme non-trivial, although most of the results presented in this section comprise comparisons of κ_{eff} between ensemble members.
2. This analysis is based on potential density with reference to a 2000 dbar pressure, whereas isoneutral mixing in the model is along local neutral surfaces, so there will be some leakage of isoneutral mixing into the diapycnal direction. As noted in the Appendix, this is not likely to be significant in global means.
3. As already stated, the contributions to density transformation from cabbeling and thermobaricity are neglected.
4. Lastly, the evaluation of κ_{eff} using offline five-day means, instead of than calculating it from $\Psi(\Theta, \rho)$ at runtime, has the potential to introduce errors through the neglect of correlations between

transport and density at time-scales shorter than 5 days. We shall show in the Appendix that the effect of offline calculation of the overturning streamfunction gives rise to errors in κ_{eff} that average over time scales of more than a few months to values that are small compared with the spread of the global mean κ_{eff} across the ensemble, and hence this approximation does not materially affect the results presented here.

4.2. Results of mixing analysis

In this section we use the analysis described in the foregoing section to investigate the sensitivity of the mixing, as represented by the effective diffusivity κ_{eff} , to tidal forcing and to the vertical coordinate. As a baseline for the analysis of the numerical mixing, we also compare κ_{eff} with the explicit diffusivity κ_{exp} used in the TKE mixing scheme, again evaluated as zonal means on potential density classes. We shall address two principal questions: firstly, what is the sensitivity of the numerical mixing to tidal forcing; and secondly, how does changing to the $z\sim$ vertical coordinate affect the numerical mixing?

We first look at the sensitivity of the explicit diffusivity κ_{exp} to the choice of the vertical coordinate and to tidal forcing. In Fig. 6 we show the zonal mean explicit diffusivity κ_{exp} , evaluated over the last 10 years of selected simulations, along with their ratios. In the top panels we compare κ_{exp} in three experiments using z^* : panels (a) and (b) show that there is relatively weak sensitivity of κ_{exp} to tidal forcing when the Simmons et al. (2004) mixing parameterisation is applied, but that when the latter is disabled (panel (c)) there is a substantial reduction in the diffusivity, especially at higher densities. Fig. 6(d), showing the ratio of κ_{exp} between the non-tidal experiments *zstar_notide* and *ztilde_5_notide*, confirms that $z\sim$ has little effect on the explicit diffusivity. Fig. 6(e) shows the ratio of κ_{exp} between *zstar_notide* and *zstar_tide*, demonstrating that tidal forcing does have a small influence on the effective diffusivity, possibly through the dependence of κ_{exp} on the vertical shear through the Richardson number in the TKE mixing scheme (see Gaspar et al., 1990). Panel (f) shows the reduction in κ_{exp} that results from disabling the Simmons et al. parameterisation, confirming that applying the latter enhances the diffusivity in almost all locations by up to an order of magnitude, with its main contributions in deep and bottom waters with σ_2 greater than 36.8 kg m^{-3} , and also in lighter waters within a band around the Equator between 15°S and 15°N .

It is useful at this point to compare the explicit diffusivities shown in Fig. 6 with those estimated from ocean observations. Waterhouse et al. (2014) use a range of turbulent mixing data to estimate the diffusivity κ , summarizing that κ rises to above $5 \times 10^{-5} \text{ m}^2 \text{ s}^{-1}$ in the bottom 1000 m over rough topography and ridges. Simmons et al. (2004) suggest that κ increases from $\sim 1 \times 10^{-5} \text{ m}^2 \text{ s}^{-1}$ at intermediate depths to $\sim 1 \times 10^{-4} \text{ m}^2 \text{ s}^{-1}$ in bottom waters. We infer that the explicit diffusivity κ_{exp} used in the present model with the Simmons et al. parameterisation (Fig. 6(a)) has a distribution much closer to observed estimates than when this scheme is not applied (Fig. 6(c)).

Fig. 7 shows ratios of the zonal mean effective diffusivity κ_{eff} , as defined in Eq. (2), between selected pairs of the experiments. The long black dashed lines indicate the maximum monthly surface density at any latitude over the analysis period; this defines the upper limits of the region of the ocean that is never part of the mixed layer, so is not subject to surface buoyancy fluxes, and in which the assumption made in Eq. (2), namely that diffusion dominates density changes, is therefore expected to hold to first order. For this reason, the diffusivity is masked out in regions where the density is lower than the maximum surface density. White areas in the interior, unventilated region (principally south of 40°S and in deep waters north of 30°N) indicate negative values of κ_{eff} , which are likely to correspond to regimes where density transformation rates from cabbeling or thermobaricity are significant compared with those from diffusion (see Section A3 of the Appendix for further discussion). The vertical bands in Fig. 7 may be associated with truncation errors from the 5-day time sampling (see Section A4 of the Appendix):

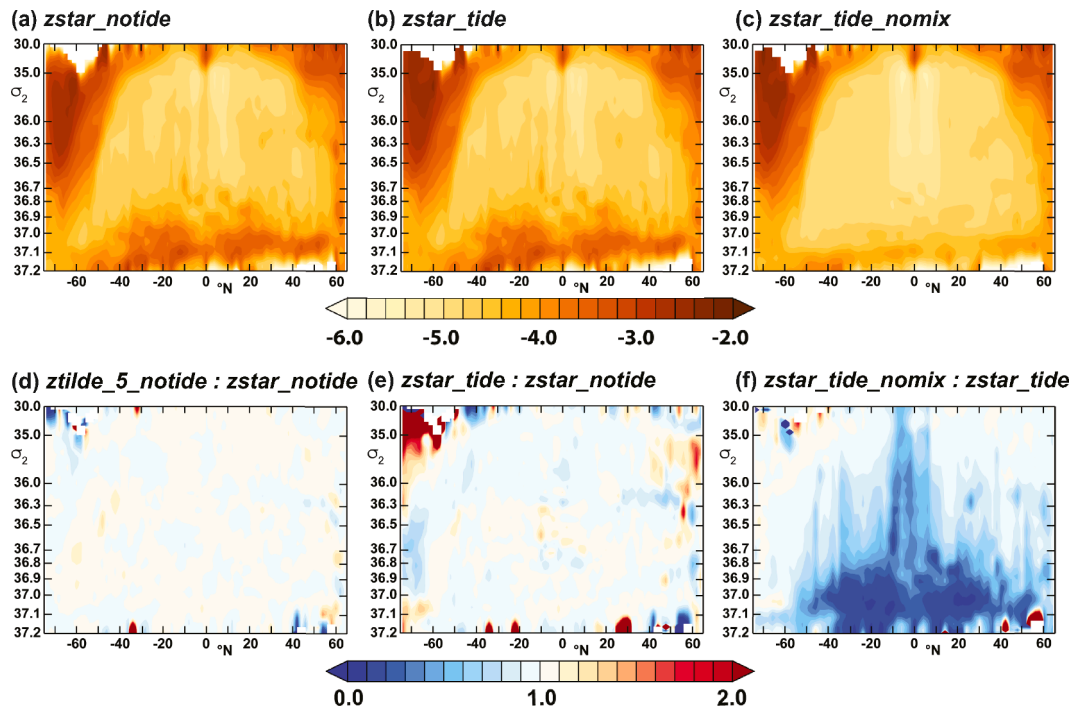


Fig. 6. The logarithm of the zonal mean explicit diffusivity κ_{exp} in the global domain, plotted against latitude and potential density σ_2 , in (a) *zstar_notide*, (b) *zstar_tide*; and (c) *zstar_tide_nomix*; and ratios of κ_{exp} between that in (d) *ztilde_5_notide* to *zstar_notide*; (e) *zstar_tide* to *zstar_notide*; and (f) *zstar_tide_nomix* to *zstar_tide*.

we also note that such features have been found to be stronger when monthly, rather than 5-day means, are used (not shown here). The results for the global means of κ_{eff} in density classes that we shall present in Fig. 8 will better represent large-scale changes in the effective diffusivity.

The top row (Fig. 7(a–c)) shows the ratios of κ_{eff} in the non-tidal experiments to that in *zstar_notide*, and the second row (panels (d–f)) shows the corresponding ratios for the three main tidal experiments; in both cases we include for comparison the trivial unity ratio between the respective z^* experiment and itself (left hand panels). In the non-tidal simulations (top panels) a general tendency is seen for $z\sim$ to reduce κ_{eff} over much of the domain, with the effect strengthening as the $z\sim$ filter timescale τ_{\sim} is lengthened from 5 days (panel (b)) to 20 days (panel (c)). A similar sensitivity to $z\sim$ is seen for the tidal simulations (panels (d–f)), with reductions in κ_{eff} being found almost everywhere. The bottom row (panels (g–i)) shows the ratio of κ_{eff} between tidal and non-tidal experiments with each of the three vertical coordinate choices: although bands of both increased and reduced κ_{eff} are seen, and the overall sensitivity is not as clear-cut as that with $z\sim$, the tendency is for tides to increase κ_{eff} within the latitude band 30°S – 30°N and at densities of $\sigma_2=35.0$ to 36.5 kg m^{-3} , the latter corresponding in this latitude range to a depth of about 1,000 metres. This is confirmed quantitatively by Table 4, which lists the mean values of κ_{eff} in this latitude and density range, along with the ratios between tidal and non-tidal pairs for each vertical coordinate choice: with z^* , tides increase κ_{eff} by 42 %, but with $z\sim$ with 20/60 day timescales the increase drops to 6 %. We note that the region between 30°S and 30°N was identified in Section 3.2 as the location of the strongest semidiurnal internal tides, as well as being the latitude range in which the diurnal internal tides are able to propagate.

To compare more quantitatively the sensitivity of the explicit and effective diffusivities to tidal forcing and to the choice of vertical coordinate, Fig. 8 shows the global means of the explicit and effective diffusivities in density classes; we include the two additional experiments *zstar_tide_nomix* (with the Simmons et al. mixing parameterisation disabled: red line), and *zstar_notide* 16 m (no tidal forcing, but with the same bathymetry as in the tidally forced experiments: cyan line) for comparison. The global means exclude the ventilated regions masked

out in Fig. 7. In the top panels we display the explicit diffusivity κ_{exp} : panel (a) shows κ_{exp} in m^2s^{-1} for each experiment on a logarithmic scale, and panel (b) shows the ratio of κ_{exp} to that in the *zstar_notide* control experiment. This confirms that in all cases except *zstar_tide_nomix* there is little sensitivity of the explicit diffusivity to either tidal forcing or to the vertical coordinate, although the tidally forced experiments (green traces and dashed blue trace) generally have a κ_{exp} smaller by between 2 % and 5 % compared with the non-tidal experiments. In *zstar_tide_nomix* (red trace), by contrast, there is a substantial reduction in the explicit diffusivity in all density classes, being about 20 % of that in *zstar_tide* in intermediate waters, dropping to less than 50 % in densities higher than $s_2 = 36.7$.

Panel (c) shows the global mean κ_{eff} in each experiment, while panel (d) shows the ratio of κ_{eff} in each experiment to that in *zstar_notide*. It can be seen that applying tidal forcing to z^* (solid green line) tends to increase the global mean κ_{eff} in density classes between $s_2 = 34.0$ and 36.7 kg m^{-3} , corresponding broadly to intermediate waters, consistent with the patterns seen in Figs. 7(g–i). The increase is over 10 % in densities lighter than 35.1 kg m^{-3} , but around 2–3 % at higher densities; the ratio of the global means is less than unity for $35.6 < s_2 < 36.1$, but comparison with Fig. 7(g) suggests that this is likely to result from partial cancellation between the increase in κ_{eff} in the tropics and the reduction between 30°N and 40°N . Enabling $z\sim$ in non-tidal simulations gives a modest reduction in κ_{eff} that increases from 5 to 10 % with a 5-day filter timescale (black dashed lines) to 10–15 % (magenta dashed line) with a 20-day timescale. In the presence of tidal forcing, however, the sensitivity to $z\sim$ is amplified: a 5-day timescale (green dashed lines) reduces κ_{eff} by more than 10 % relative to *zstar_tide*, while $z\sim$ with a 20-day timescale (blue dashed lines) produces a reduction in κ_{eff} of more than 20 %. As a result, the combination of tides and $z\sim$ with a 20-day timescale has, perhaps surprisingly, between 15 and 30 % less mixing than with the non-tidal z^* simulation *zstar_notide*, with the largest reductions at densities between $s_2 = 36.5$ and 36.7 kg m^{-3} , typical of Upper North Atlantic Deep Water, and between $s_2 = 36.9$ and 37.1 kg m^{-3} , corresponding to bottom waters. Disabling the Simmons et al. mixing parameterisation in *zstar_tide_nomix* (solid red line in panels (c) and (d)) gives a robustly smaller κ_{eff} than in *zstar_tide* (solid green line),

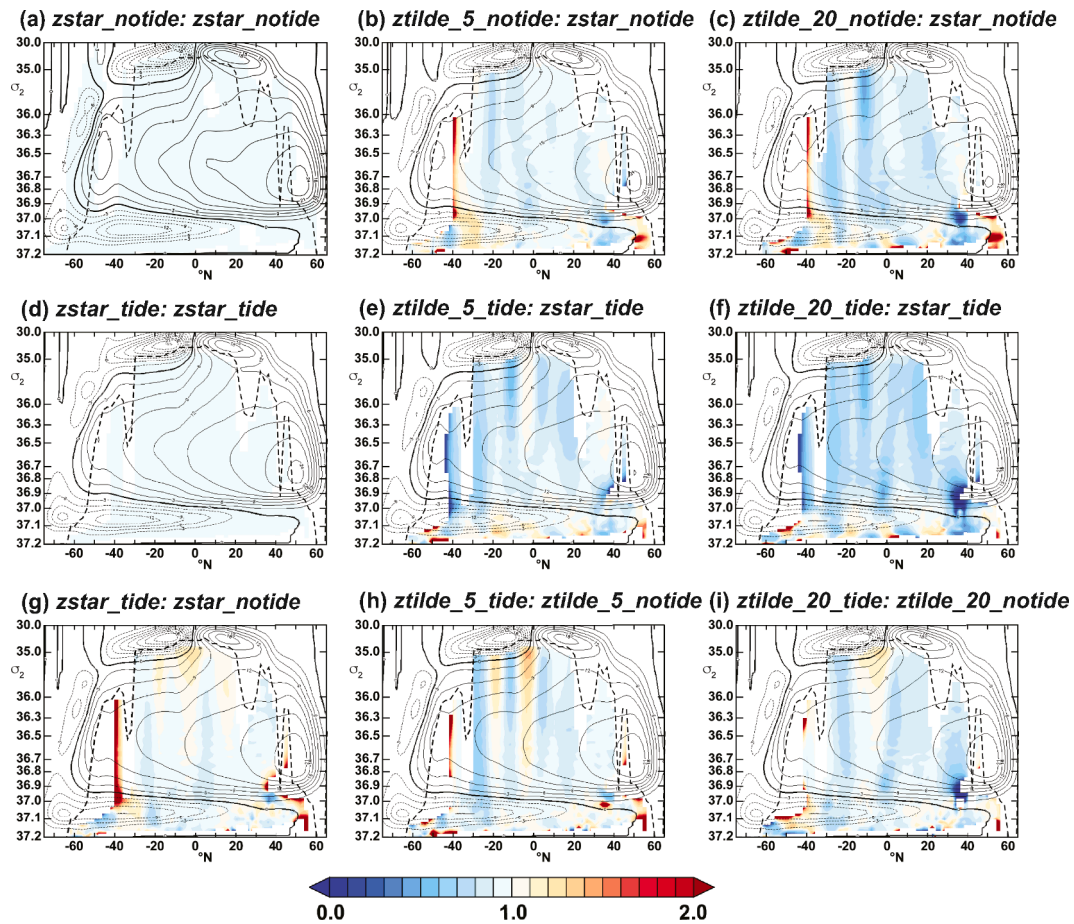


Fig. 7. Ratios of the effective diffusivity κ_{eff} in the global domain to that in *zstar_notide*, plotted against latitude and potential density s_2 . Ratios to *zstar_notide* of: (a) *zstar_notide*; (b) *ztilde_5_notide*; (c) *ztilde_20_notide*; ratios to *zstar_tide* of: (d) *zstar_tide*; (e) *ztilde_5_tide*; and (f) *ztilde_20_tide*; and ratios between tidal and non-tidal experiments with (g) z^* ; (h) $z\sim$ with a 5-day timescale; and (h) $z\sim$ with a 20-day timescale. The long dashed black lines show the maximum monthly surface density over the analysis period, and the black contours are of the global overturning streamfunction. Values of κ_{eff} are masked out where the density is less than the maximum monthly surface density at that latitude.

which is chiefly attributed to the reduction in the baseline physical mixing.

We note that in some density and latitude ranges the effective diffusivity is less than the explicit diffusivity; in particular, at densities greater than $s_2 = 36.9$ the effective diffusivity is generally smaller than κ_{exp} , corresponding to values less than unity in Fig. 8(e). This may result at least partially from the small κ_{eff} values close to the zero crossing between 40°S and 50°S (negative values are masked in these figures), which correspond to the large positive and negative ratios in this region seen in Fig. 7, particularly at densities greater than $s_2 = 36.9$. In addition, as discussed in Appendix A, comparisons between explicit and effective diffusivities are not altogether robust, because of the approximation made in zonally averaging the vertical density gradient in Eq. (2), so the ratios below unity may not be significant.

Finally, the deepening of the bathymetry found to be necessary for the tidally forced simulations has a negligible effect on either the explicit or effective diffusivities when applied to the non-tidal experiment *zstar_notide_16 m* (solid cyan curves in Fig. (8)).

5. Sensitivity of model fields to $z\sim$ and tidal forcing

5.1. Changes in thermocline stratification

Changes in net mixing would be expected to manifest as changes in the density stratification. As a measure of the stratification, we use the square of the buoyancy frequency $N^2 = -\frac{g}{\rho_0} \frac{\partial \rho}{\partial z}$ where $g = 9.81 \text{ m s}^{-2}$

and $\rho_0 = 1035 \text{ kg m}^{-3}$. In Fig. 9 we show the ratios of this quantity between each experiment and that in *zstar_notide*, evaluated in each case from monthly means over the ten-year analysis period at the thermocline depth, here defined as the maximum value of N^2 in the upper 1000 m. In the non-tidal experiments (panels (a–c)), the sensitivity of N^2 at the thermocline to $z\sim$ is relatively weak over most of the ocean, with the exception being a marked increase in the northwest Atlantic and changes of both signs in the Southern Ocean. This is qualitatively consistent with Fig. 7(b) and (c), which show that the effective diffusivity just below the ventilated region, shown by the black dashed lines, is relatively weakly sensitive over much of the ocean to the choice of vertical coordinate. Tidal forcing (panels (d–f)) consistently reduces the stratification in the thermocline by 10–20 % with the exception again being in the Southern Ocean, with the largest large-scale reductions seen between 30°S and 30°N ; this is the latitude range where the maximum internal tide is found (Fig. 2), as well as where an increase in κ_{exp} was noted in Fig. 7(g–i). To summarize, the effect of tides is principally to reduce the stratification at the thermocline, and changing from z^* to $z\sim$ increases the stratification.

5.2. Temperature biases and drifts

Biases in the temperature and salinity in a given ocean model configuration can develop for a number of reasons, including errors in surface forcing, biases in the overturning or gyre circulations, inappropriately tuned mixing parameterisations, as well as spurious numerical

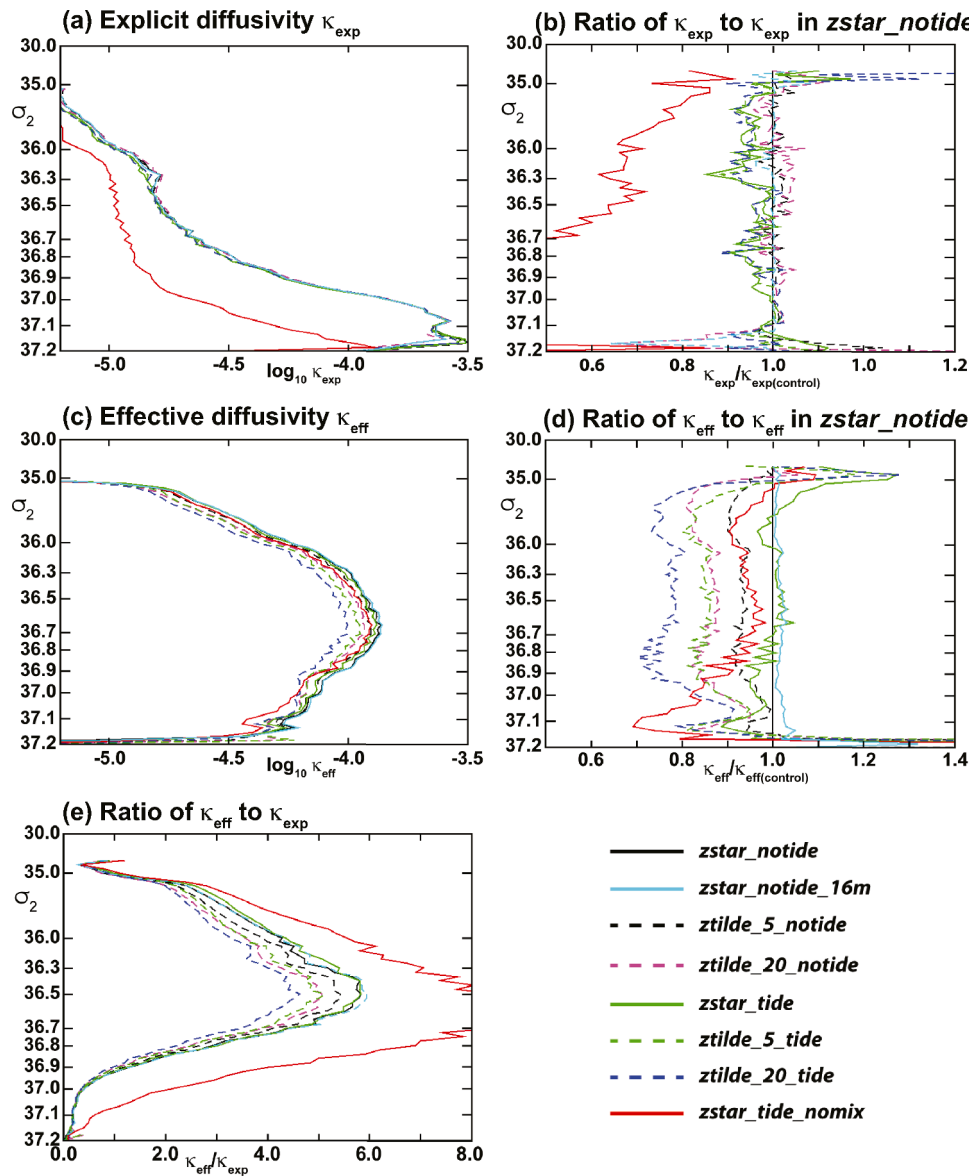


Fig. 8. Global volume-weighted mean diffusivities and their ratios, evaluated in potential density classes: (a) log of global mean explicit diffusivity κ_{exp} ($\text{m}^2 \text{s}^{-1}$); (b) ratios of global mean explicit diffusivity κ_{exp} to that in *zstar_notide*; (c) log of global mean effective diffusivity κ_{eff} ($\text{m}^2 \text{s}^{-1}$); (d) ratios of κ_{eff} to that in *zstar_notide*; (e) ratios of effective diffusivity κ_{eff} to the respective explicit diffusivity κ_{exp} .

Table 4

Mean values of the effective diffusivity κ_{eff} in the latitude range 30°S to 30°N , and over values of s_2 between 35.0 and 36.5 kg m^{-3} .

Run	Mean κ_{eff}	$\kappa_{\text{eff}}(\text{tide}) / \kappa_{\text{eff}}(\text{no tide})$
<i>zstar_notide</i>	3.902×10^{-5}	–
<i>ztilde_5_notide</i>	4.990×10^{-5}	–
<i>ztilde_20_notide</i>	5.565×10^{-5}	–
<i>zstar_tide</i>	5.546×10^{-5}	1.42
<i>ztilde_5_tide</i>	5.653×10^{-5}	1.13
<i>ztilde_20_tide</i>	5.923×10^{-5}	1.06

mixing. There is also the potential for compensating errors, so that correcting one may worsen the realism of the model (e.g. Hyder et al., 2018). In a small ensemble of a single configuration, it is non-trivial to disentangle the possible causes of biases, but MCS2022 demonstrated a robust correlation between the level of numerical mixing and zonal mean temperature biases, with reductions in the former consistently reducing the latter. This reduction was most pronounced at a depth of

300–500 m, typical of the seasonal thermocline; in that ensemble, lengthening the $z\sim$ time scales led to progressively increased warming at mid-latitudes and cooling in the North Pacific and Southern Ocean, with both these tendencies opposing the large-scale biases in the z^* control. Fig. 10 shows the zonal mean temperature bias in the present ensemble, averaged over 1996–2005 with respect to the EN4 climatology (Good et al., 2013) at selected depth levels, which may be compared directly with Fig. 8 of MCS2022. The effect of $z\sim$ in the non-tidal experiments (black and magenta lines) is to reduce both the cold bias between 30°S and 30°N and the warm bias between 30°N and 60°N ; the effect is similar in magnitude at 300 m and 500 m and less at 1000 m, and weak at the surface and deeper than 1000 m. The effect of tidal forcing with both z^* and $z\sim$ (green and blue curves) is, perhaps surprisingly, to further oppose the biases in these same depth ranges, with a strong additional warming of 0.3–0.4 K between 30°S and 30°N at 300 m and a cooling by a similar amount between 40°N and 60°N . The combination of tides and $z\sim$ (green and blue dashed lines) gives the largest change from *zstar_notide*, with *ztilde_20_tide* in fact reversing the sign of the bias at low latitudes to give a slightly positive zonal mean

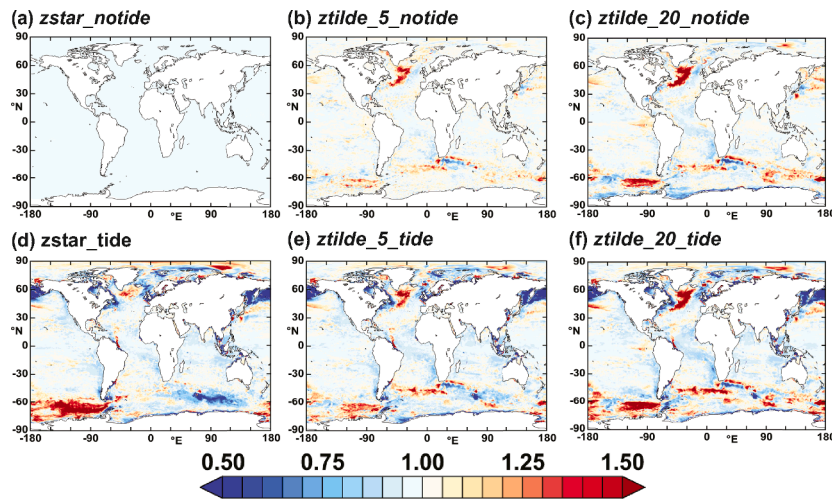


Fig. 9. Ratios of the square of the buoyancy frequency N^2 at the depth of the thermocline to that in $zstar_notide$ of (a) $zstar_notide$; (b) $ztilde_5_notide$; (c) $ztilde_20_notide$; ratios to $zstar_tide$ of (d) $zstar_tide$; (e) $ztilde_5_tide$; and (f) $ztilde_20_tide$.

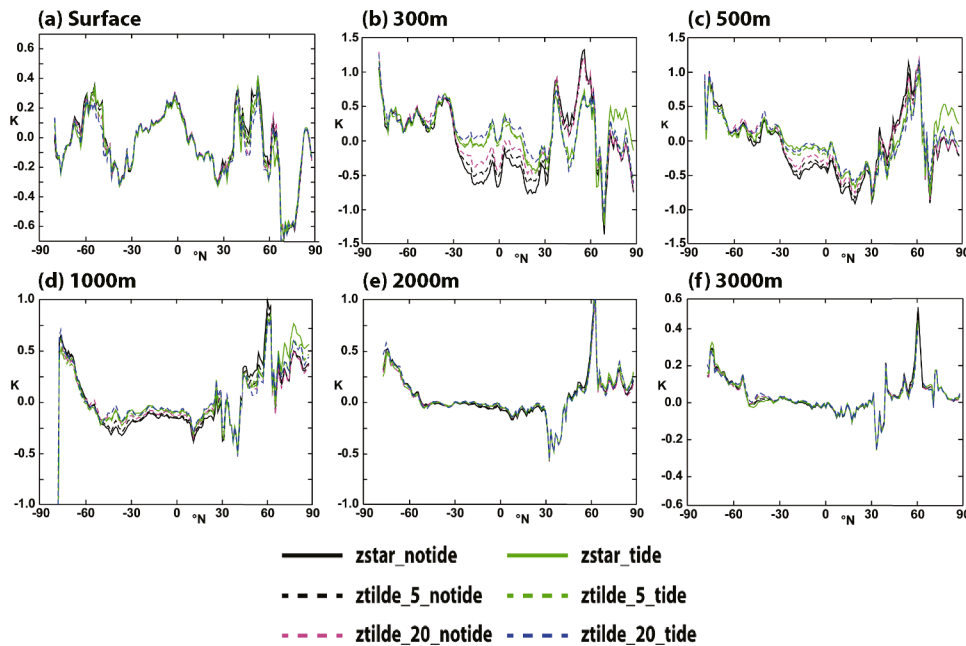


Fig. 10. Zonal mean temperature biases at selected depth levels, with respect to the mean over the same time period in the EN4 climatology: (a) surface; (b) 300 m; (c) 500 m; (d) 1000 m; (e) 2000 m; and (f) 3000 m.

bias. At latitudes north of 70°N , tidal forcing in the z^* case causes a significant warm bias at depths between 300 m and 2000 m (solid green lines in Figs. 10(b)-(d)) that is strongly reduced by $z\sim$, which reduces the mean biases to close to zero.

Table 5
Global RMS temperature biases in K with respect to the EN4 climatology in years 1996–2005.

Run	0m	300m	500m	1000m	2000m	3000m
$zstar_notide$	0.569	0.807	0.619	0.316	0.130	0.095
$ztilde_5_notide$	0.568	0.766	0.602	0.302	0.124	0.091
$ztilde_20_notide$	0.567	0.742	0.587	0.295	0.120	0.089
$zstar_tide$	0.559	0.747	0.552	0.285	0.124	0.090
$ztilde_5_tide$	0.566	0.720	0.555	0.296	0.122	0.088
$ztilde_20_tide$	0.569	0.724	0.554	0.293	0.127	0.092
Standard dev (% of $zstar_notide$ mean)	0.6 %	3.7 %	4.5 %	3.2 %	2.7 %	2.3 %

Table 5 lists the global RMS biases on each of these depth levels, as well as the ratio of the respective standard deviation to the ensemble mean at each depth. At the surface the biases differ by less than 1 % across the ensemble: this lack of sensitivity is mainly due to the feedback imposed from the surface heat flux onto the SST through the bulk formulae. At 3000 m the biases and the variation across the ensemble are again small. At other depth levels, these figures confirm the pattern observed qualitatively earlier in the section: firstly, that the biases consistently reduce from $zstar_notide$ to $ztilde_5_notide$ and further to $ztilde_20_notide$, and secondly that tidal forcing further reduces the biases, although among the tidally forced experiments the sensitivity to the vertical coordinate is not significant.

To display the spatial structure of the changes from $z\sim$ and tides, and to confirm the consistency of the reduction in temperature bias, Fig. 11 shows the biases in the z^* control $zstar_notide$ at 300 m and 2000 m, and the changes at the same depths in each of the other five simulations relative to $zstar_notide$. At 300 m (Fig. 11(a)) large-scale warm biases of

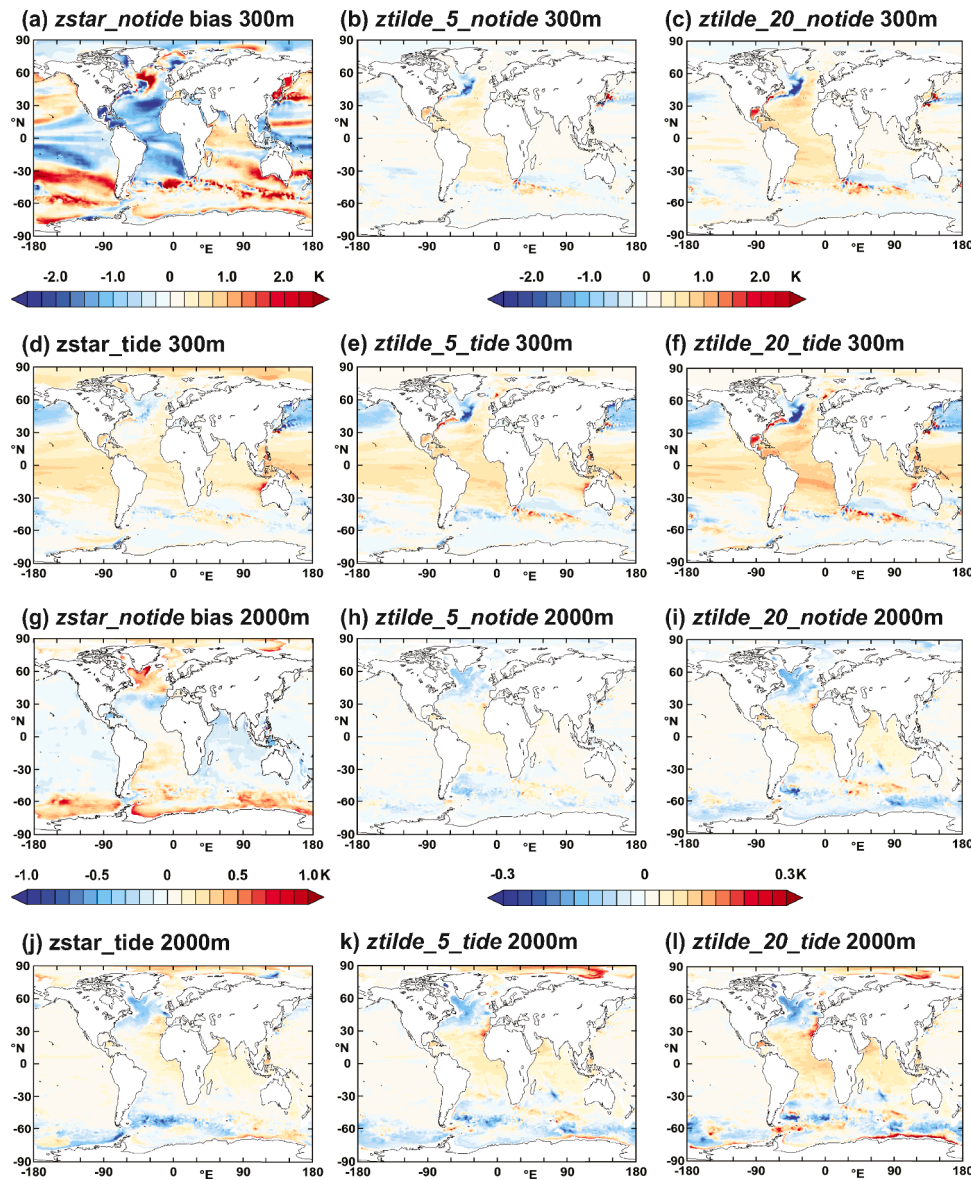


Fig. 11. Temperature biases in K, averaged over 1996–2005, at two selected depth levels, and the sensitivity of the temperature to $z\sim$ and tidal forcing. (a) the temperature bias at 300 m in *zstar_notide* with respect to the EN4 climatology; the temperature change at 300 m from *zstar_notide* in (b) *ztilde_5_notide*; (c) *ztilde_20_notide*; (d) *zstar_tide*; (e) *ztilde_5_tide*; and (f) *ztilde_20_tide*. (g) the temperature bias at 2000 m in *zstar_notide* with respect to the EN4 climatology; the temperature change at 2000 m from *zstar_notide* in (h) *ztilde_5_notide*; (i) *ztilde_20_notide*; (j) *zstar_tide*; (k) *ztilde_5_tide*; and (l) *ztilde_20_tide*. The left-hand colour legends apply to the temperature biases with respect to climatology at the respective depth, and those at centre right apply to the temperature changes with respect to the *zstar_notide* control experiment.

up to ± 2 K are clearly visible in the subpolar gyres of the Pacific and Atlantic and in the Southern Ocean, along with cold biases of similar magnitude in the subtropical and tropical regions. The exception to the latter is the Indian Ocean, where there is a warm bias of around 0.5 K. Enabling $z\sim$ (Fig. 11(b) and (c)) partially reverses these biases, with a relatively stronger effect in the subtropical and tropical Atlantic, and lengthening the $z\sim$ timescales (Fig. 11(c)) gives a stronger reduction than with the default settings. As remarked by MCS2022, $z\sim$ causes an enhancement of the cold bias off Newfoundland, which may be related to partial cancellation of a structural error in the path of the separated Gulf Stream related to the $1/4^\circ$ resolution (e.g. Marzocchi et al., 2015). Adding tidal forcing to z^* (Fig. 11(d)) leads to a warming of almost 1 K in those tropical and subtropical regions where *zstar_notide* shows a cold bias, with larger changes seen in the tropical Pacific, where $z\sim$ alone has a relatively weak effect. At this depth tidal forcing also has a cooling effect of 0.5–1.0 K across the whole latitude band between 30°N and

60°N where *zstar_notide* is biased warm. Enabling $z\sim$ with tidal forcing (Figs. 11(e) and (f)) combines the effects of the two changes almost linearly: in the South Atlantic and the tropical Pacific, *ztilde_20_tide* robustly shows the largest reduction in the biases with respect to those in *zstar_notide*. In the Arctic, tidal forcing introduces a warming that almost cancels the cool bias of between 0.5 and 1.0 K in the Arctic in *zstar_notide* (Fig. 11(d)), while the combination of tides and $z\sim$ in *ztilde_20_tide* (Fig. 11(f)) results in little change compared to that in *zstar_notide*. The temperature at 300 m in the Southern Ocean has a relatively weak sensitivity to either tides or $z\sim$, although comparison of Fig. 11(f) with Fig. 11(a) confirms that the overall cooling of about 0.5 K from the combination of tides and $z\sim$ with $t_{\sim}=20$ days still opposes the warm bias in *zstar_notide*.

At 2000 m similar responses to $z\sim$ and tidal forcing are seen, albeit to a much lower extent: the biases in *zstar_notide* (Fig. 11(g)) have a similar overall structure, being up to 1 K warmer than EN4 in the Arctic and the

Southern Ocean and 0.2–0.3 K cooler in the Pacific and Indian Oceans and in the North Atlantic, although while at 300 m the South Atlantic region is over 1 K cooler than the climatology at 2000 m it shows a warm bias of 0.2–0.4 K. The changes in temperature at 2000 m depth with tidal forcing and $z\sim$ are similar in spatial extent, if again weaker, to those at 300 m, and again generally tend to oppose the biases in the $zstar_notide$ control. The exceptions are in the South Atlantic and in the Arctic, where the warm bias in the control is enhanced in $ztilde_20_tide$. In contrast to the case at 300 m, $z\sim$ does not strengthen the biases in the North Atlantic subpolar gyre at 2000 m.

5.3. Large-scale circulation

MCS2022 demonstrated that implementing $z\sim$ with progressively longer timescale parameters led robustly to a weakening by up to 1.5 Sv in the maximum overturning circulation (AMOC) at 26°N, which was well correlated with the global mean of the effective diffusivity k_{eff} for each selection of the timescale parameters. This was interpreted as a causal link between the strength of mixing in both mid-latitudes and the Southern Ocean and the strength of the overturning (in other words, a larger rate of mixing is associated with a stronger AMOC), which has been recognized through modelling and observational studies for several years (Bryan 1987; Scott and Marotzke 2002; Webb and Sugihara, 2001; Cimoli et al., 2023). Fig. 12(a) and (b) show the evolution of the AMOC strength at 26°N and 45°N in the present ensemble, while columns 2 and 3 of Table 6 list the mean strength of the AMOC at these latitudes over years 21–30 of each of the integrations. The sensitivity to tides and the choice of vertical coordinate is clearer at 26°N than at 45°N; at the former latitude, there is a clear tendency for the overturning to weaken, both with and without tides, as the $z\sim$ timescales are lengthened: in both $ztilde_20_60_notide$ and $ztilde_20_60_tide$ there is a weakening of the AMOC by about 6 % compared with the respective z^* experiment. The difference between non-tidal and tidally forced experiments, with corresponding choices of the vertical coordinate, are much

Table 6

Circulation indices in the model simulations, evaluated from annual means over the period 1996–2005: overturning strength at 26°N; overturning strength at 45°N; Antarctic Circumpolar Current (ACC) transport through Drake Passage; and Indonesian Throughflow (ITF), all in Sv.

	AMOC at 26°N	AMOC at 45°N	ACC transport	ITF
<i>zstar_notide</i>	21.50	18.03	125.3	-18.6
<i>ztilde_5_30_notide</i>	20.78	17.91	127.5	-17.9
<i>ztilde_20_60_notide</i>	20.22	18.01	130.7	-17.5
<i>zstar_tide</i>	21.21	18.12	119.1	-18.7
<i>ztilde_5_30_tide</i>	20.91	19.81	129.2	-17.7
<i>ztilde_20_60_tide</i>	20.02	17.86	128.0	-17.2
<i>zstar_tide_nomix</i>	21.65	18.33	114.1	-18.5

smaller. It is of interest to note that the experiment *zstar_tide_nomix* with the Simmons et al. mixing parameterisation disabled (cyan line) has an AMOC strength at 26°N that is close to that in *zstar_tide*, which suggests that either other interior processes besides mixing influence the overturning strength, or that the mixing that strengthens the overturning occurs in regions where the enhancements to the diffusivity contributed by the tidal parameterisation scheme are not large. Another possible reason is that the parameterised mixing scheme and numerical mixing from the tides will certainly change the spatial structure of the diffusivity (both explicit and numerical) in different ways and therefore the induced water-mass transformation.

The Antarctic Circumpolar Current (ACC) transport through the Drake Passage in *zstar_notide* (the solid black line in Fig. 12(c)) spins down from the first year by about 25 Sv over the 30-year integration, while in the absence of tidal forcing $z\sim$ consistently reduces the spin-down by between 3 and 5 Sv. Adding tidal forcing (green solid line) substantially weakens the transport, but $z\sim$ in this case reverses the weakening, and in *ztilde_20_tide* the ACC is about 3 Sv stronger than in the *zstar_notide* control (Table 6). Disabling the tidal mixing parameterisation (solid cyan line leads to the weakest ACC transport of the

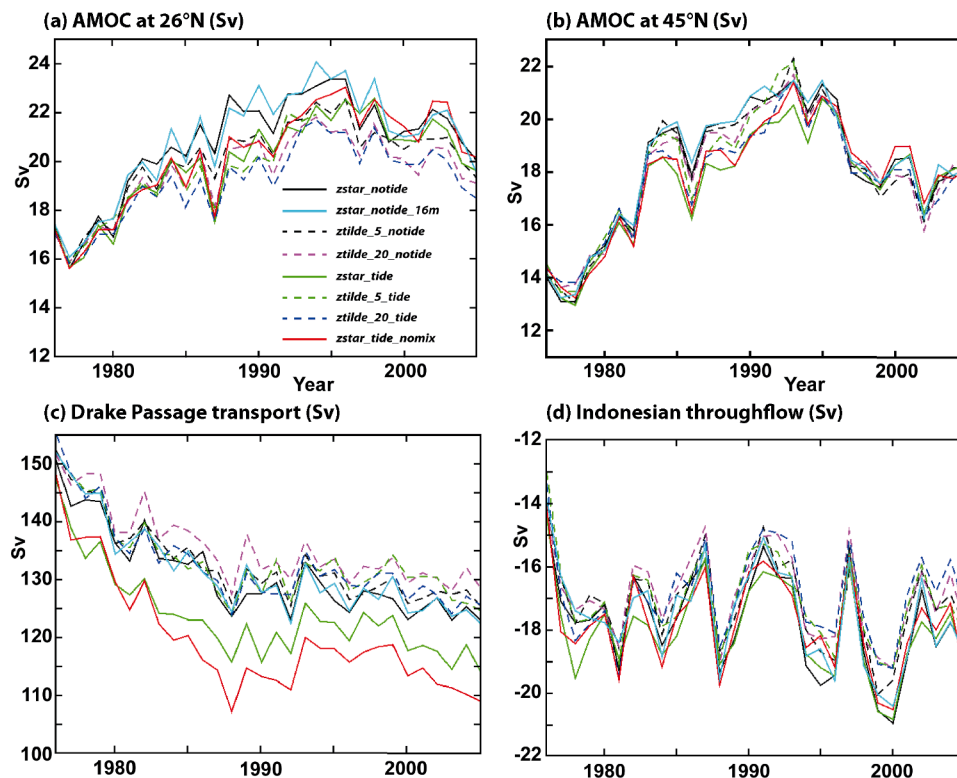


Fig. 12. Large-scale annual circulation indices in Sv in the model simulations: (a) overturning strength at 26°N; (b) overturning strength at 45°N; (c) transport through Drake Passage; and (d) Indonesian throughflow.

ensemble. We conclude that applying tidal forcing to this configuration along with $z\sim$ with a 20-day timescale gives a modest improvement to the ACC transport, which is comparable to the ~ 3 Sv of strengthening reported by Megann and Storkey (2021) when the viscosity was increased in a similar configuration.

The total throughflow through the Indonesian Archipelago (ITF) from the Pacific to the Indian Ocean between 2004 and 2006 was estimated under the INSTANT observational program to be 15.0 Sv with a seasonal cycle of about 2 Sv (Sprintall et al., 2009). Sasaki et al. (2018) report an increase in the ITF in a 0.1° near-global model when a tidal mixing parameterisation is applied. Katavouta et al. (2022) used a $1/12^\circ$ regional NEMO model to investigate the sensitivity of the Indonesian throughflow to tidal forcing, reporting a small increase in throughflow of about 1 Sv with tides, and conclude that the main contribution to the change in the net transport arose from interactions between the barotropic tide and the mean stratification in the straits. In the *zstar_notide* control experiment the mean ITF (see Fig. 12(d) and Table 6) is 18.6 Sv; this suggests that the throughflow is a little stronger than the observational estimate, but the significant interannual variability of about ± 2 Sv seen in the simulations makes direct comparison with the three-year INSTANT observational time series less useful. Adding tidal forcing with z^* slightly strengthens the ITF by 0.7 %, while $z\sim$ consistently weakens the transport by between 5 % and 7.5 %. These results are consistent with the modelling studies cited above, and we conclude firstly that tidal motions strengthen the ITF by increasing mixing, mainly due to the barotropic tide; and secondly that $z\sim$ weakens it by reducing numerical mixing.

5.4. Sensitivity of sea ice to tides and $z\sim$

As noted in the Introduction, sensitivity of the seasonal sea ice extent to tidal forcing has been reported in polar regions in model studies (e.g. Luneva et al., 2015). Fig. 13 shows the mean seasonal cycle of ice extent and volume, averaged over the ten-year period 1996–2005, in the northern and southern hemispheres, along with estimated observational bounds (± 20 %) from the HadISST climatology (Rayner et al., 2003) for ice extent, and from the PIOMAS reanalysis (Zhang and Rothrock, 2003) for ice volume (Northern hemisphere only), respectively. The *zstar_notide* control, like the preceding GO6 configuration (see Fig. 13 of Storkey

et al., 2018) has a realistic winter sea ice cover in both hemispheres (the solid black line in Fig. 13(a) and (b)), compared with observations, but excessively low sea ice extent in the summer, whereas the sea ice in the Arctic is too thin all year round, as evidenced by the sea ice volume (Fig. 14(c)), which is below the lower observational bound for almost all months. The effect of tides (green and blue lines in Fig. 13) is to reduce the ice cover in the Arctic, but the sensitivity is weak, with a reduction of less than 4 % in the March ice cover in the Arctic in *zstar_tide* relative to that in *zstar_notide*, and less than 1 % in the September ice cover in the Antarctic. The sensitivity to tides of the northern hemisphere sea ice volume is negligible, as is that of both the extent and volume in the southern hemisphere (Figs. 13(b) and (d)). Finally, none of the metrics is significantly affected by changing to $z\sim$: for example, winter sea ice extent in both hemispheres is changed by less than 0.1 % between *zstar_notide* and *ztilde_20_notide*. Although the changes are small compared with those reported by Luneva et al. (2015) and others, they are not unsurprising, given that the sea ice is predominantly controlled by the atmospheric fluxes, particularly at this relatively coarse resolution.

6. Summary and discussion

We have implemented tidal forcing, using the five harmonics M2, S2, N2, O1 and K1, in a global forced $1/4^\circ$ NEMO configuration, and have created an ensemble of simulations with the aim of assessing the numerical mixing due to the tides. We have included for comparison both the default z^* geopotential coordinate and the filtered arbitrary-Lagrangian-Eulerian $z\sim$ coordinate, which represents the vertical motions of internal waves with period of less than a few days as displacements of the coordinate surfaces, rather than as advective vertical velocities relative to the coordinate surfaces, and which has previously been shown (Megann et al., 2022) to significantly reduce numerical mixing from internal waves in non-tidal simulations. We have confirmed that the external tide, represented by harmonics of the surface elevation at the tidal forcing frequencies, is acceptably realistic in amplitude and phase in all the simulations, despite the relatively low horizontal resolution. We have diagnosed the internal tide, as represented by its signature in the surface elevation, and confirmed that this is broadly similar to that seen in satellite altimetry and in high-resolution tidal

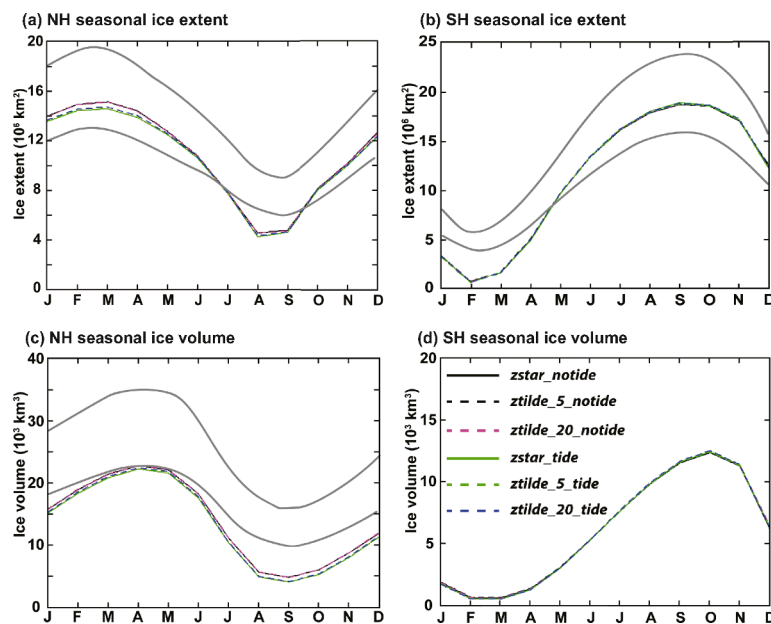


Fig. 13. Mean seasonal cycle of monthly sea ice extent and thickness over 1996–2005 of the main ensemble: ice extent in km^2 in the (a) northern and (b) southern hemispheres; and ice volume in km^3 in the (c) northern and (d) southern hemispheres. The grey solid lines indicate the estimated observational bounds, derived from the respective dataset as described in the text.

models, albeit being significantly weaker than that in either of the latter, and that its propagation away from the generation regions is realistically represented. Finally, the amplitude and spatial structure of the surface signature of the internal tides are not significantly affected by the choice of vertical coordinate in the model.

We have examined the internal structure of the internal tides in the simulations and its sensitivity to the vertical coordinate: they are present almost exclusively in the first vertical mode, as expected, given the horizontal resolution of the model grid, and are characterized in the z^* case by a maximum vertical velocity at around 2000 metres depth. When the z^* vertical coordinate is replaced by z_{\sim} , the Eulerian vertical velocity corresponding to the internal tide is progressively transformed into displacements of the coordinate surface as the z_{\sim} timescale is lengthened, and with a 20-day timescale the Eulerian velocity from tidal motions is reduced to less than 10 % of its amplitude with z^* .

The effects of tidal forcing and of the choice of vertical coordinate on mixing were quantified using a mixing analysis based on density transformation rates to derive an effective diapycnal diffusivity k_{eff} for each of the experiments. In summary, tidal forcing in the z^* experiments led to an increase of up to 20 % in the effective diffusivity in density classes corresponding to thermocline and intermediate waters and at latitudes between 30°S and 30°N, where a strong internal tide is present, but changing to the z_{\sim} vertical coordinate produced a strong reduction in diagnosed mixing both with and without tides and, perhaps surprisingly, the experiments with tides and z_{\sim} showed effective diffusivities between 15 % and 25 % lower than in the non-tidal z^* control experiment over intermediate and deep water densities. The sharpness of the seasonal thermocline, as represented by the maximum density stratification in the upper 1000 m, was found to be qualitatively consistent with the sensitivity of effective diffusivity to tides and the choice of vertical coordinate. The sensitivities of temperature biases at 300 m and 2000 m depths with respect to the EN4 climatology were broadly consistent with those of the mixing diagnostics: the cool biases at 300 m between 30°S and 30°N in the control were reduced by more than 50 % with tides and z_{\sim} , while the warm biases between 35° and 65°N were reduced by a comparable fraction. Similar sensitivity was seen at 2000 m depth, although the magnitudes of the biases at that depth are less than 25 % of those at 300 m. With z^* and tides a warm bias in the Arctic at 300 m of between 0.5 and 1.0 K was present, but in all the other experiments this bias was replaced by a much smaller overall cool bias. To summarize, tidal forcing with z^* increases mixing in thermocline and intermediate waters between 30°S and 30°N, reducing it slightly elsewhere, while the combination of tides and z_{\sim} reduces mixing almost everywhere, relative to that in the z^* non-tidal control.

The sensitivity of the Atlantic meridional overturning circulation (AMOC) at 26°N to tidal forcing and the vertical coordinate was proportionate to those of the mixing and the temperature biases: the AMOC was strongest in the z^* non-tidal control, and weakest with tidal forcing and with the longest z_{\sim} timescale. This confirms the hypothesis of Webb and Suginohara (2001), Wunsch and Ferrari (2004) and others that mixing is a significant control on the AMOC, in the sense that stronger mixing leads to a stronger overturning circulation. The transport through Drake Passage of the Antarctic Circumpolar Current (ACC) is characterized in the non-tidal control by a gradual spindown of 25–30 Sv from the initial transport of 150 Sv. The ACC transport has the opposite sensitivity to the AMOC, with the z^* non-tidal and tidal simulations having the largest spindown, and the tidally-forced experiment with a 20-day z_{\sim} timescale having the least, with the weakening reduced to about 20 Sv relative to the control. In that sense, this latter configuration, which we have shown to have the lowest global mean numerical mixing of the present ensemble, has the most realistic representation of the ACC. A direct link between ACC transport and numerical mixing is difficult to establish rigorously using this method, however, since the Southern Ocean is a region where the influence of cabling and thermobaricity on density transformations is significant. Nevertheless, it would be consistent with the hypothesis (e.g. Johnson

and Bryden, 1989) that the ACC is supported by a mean tilt of the isopycnals in the Southern Ocean, and that stronger mixing erodes this tilt and hence weakens the ACC. Finally, a small but robust dependence on tidal forcing was seen in the Indonesian throughflow (“ITF”), which was slightly strengthened by the addition of tides to z^* , but weakened by a few percent in the tidal experiments with z_{\sim} ; this is consistent with the results of Katavouta et al. (2022), who found that tidal forcing by itself strengthened the ITF transport by 5–6 % in their 1/12° z^* NEMO simulation.

Examination of the explicit and effective diffusivities with and without the Simmons et al. (2004) tidal mixing parameterisation confirms that the total mixing from tidal motions, including both physical and numerical contributions, in this configuration is much lower than that provided by the parameterisation, and is indeed much weaker than observational estimates for mixing. This is not surprising, since the eddy-permitting resolution used in this ensemble is far too low to simulate the higher vertical modes of the internal tide, and indeed the higher frequency internal waves that result from these internal tides, that perform mixing in the ocean. We therefore conclude that a mixing parameterisation is necessary in tidally forced simulations of this resolution, which of course is typical of climate models. The Simmons et al. scheme is not provided in standard releases of NEMO v4, and in any case has been superseded by that of de Lavergne et al. (2020), so the latter is recommended for new NEMO-based configurations.

It is not yet clear why tidal forcing with z^* slightly reduces the explicit vertical diffusivity outside the 30°S–30°N latitude range, as shown in Fig. 8(b), nor why the diagnosed numerical mixing and temperature biases are significantly reduced over much of the model domain when tides are present, particularly when combined with the z_{\sim} vertical coordinate. Candidates include a possible reduction by the barotropic or internal tide of the grid-scale vertical velocities associated with a computational mode at mid-depths close to western boundaries, as described by Megann (2018) and Megann and Storkey (2021) in related ¼° simulations, which may interact non-trivially with tidal motions; changes to viscous damping along western boundaries from the tidal currents; and changes to bottom layer thicknesses. Another possible cause could be nonlinear interactions between the internal tides and the NIGWs, which could disrupt the propagation of the latter. Further work is needed to clarify this question.

As already stated, the analysis used in Section 4 involves some approximations and assumptions, which are discussed in Appendix A, notably including the use of offline time averages and neglecting the effects of the nonlinear equation of state. We have presented evidence that suggests that the errors introduced by using 5-day time averages, when the results are evaluated over times of more than a few months, are not first-order in magnitude compared with the differences between the effective diffusivities in different simulations, so errors from this source are unlikely to materially affect the results presented in this paper. The discrepancies in the effective diffusivity from using 5-day means take the form of zonal bands of opposing sign on each side of the Equator extending to about 10°N and S, so these average to zero to first order in global means, and in the regional means shown in Table 4. Nevertheless, evaluating the volume transports in density classes during runtime would be preferable. The neglect of the effects of cabling and thermobaricity in the calculation of the effective diffusivity is only likely to have significant influence on the results in the Southern Ocean, so again does not substantially affect the comparisons described here, but further work would be necessary to directly evaluate these contributions to k_{eff} to confirm this. An approach similar to that used by Holmes et al. (2021), in which heat budgets are evaluated in individual water columns during runtime, would circumvent at least some of the limitations of the present method, and in addition gives spatial information on the locations where numerical mixing takes place.

The present configuration was created to provide a working tool to explore the effects of tidal motions on numerical mixing, and is certainly not optimized to simulate a tidally-forced ocean realistically, even

considering its limited resolution. Only five tidal constituents are applied, while the formulation of the bottom drag is likely to be sub-optimal in the presence of time-mean and tidal currents at the sea bottom. Work is ongoing under the Shelf-Enabled NEMO project, developed partly under the Mission Atlantic program (Artioli, 2023), which uses a global $1/4^\circ$ NEMO v4.0 configuration closely related to that used in the present study to improve the performance of the model on the shelves without degrading the simulation in the deep ocean. The configuration used in that project, for example, applies 23 tidal forcing constituents, and has found that a modified bottom drag scheme, which treats motions on diurnal and shorter timescales separately from lower-frequency motions, gives considerable improvements in the representation of the barotropic tide (C. Wilson, pers. comm.). Finally, the application of a tidal mixing parameterisation scheme in the presence of resolved barotropic and low-mode internal tides is unsatisfactory, since it is likely to introduce double-counting of at least some of the contributions to mixing from these sources, so further research is needed to investigate the consequences of this.

We conclude that explicit representation of tidal motions generally improves the realism of the $1/4^\circ$ NEMO configuration used here, and that changing from the z^* geopotential coordinate to the $z\sim$ filtered ALE coordinate further improves the performance of the model, mainly through its consistent effect in reducing numerical mixing from the internal tide. Our results suggest that investigating the effect of tidal forcing in the next generation of coupled climate models and Earth System Models will be worthwhile, providing that attention is paid to addressing numerical mixing through appropriate choice of the vertical coordinate.

CRedit authorship contribution statement

Alex Megann: Conceptualization, Methodology, Software, Validation, Formal analysis, Investigation, Resources, Data curation, Writing – original draft, Writing – review & editing, Visualization, Project administration, Funding acquisition.

Declaration of competing interest

The authors declare that they have no known competing financial

Appendix A. Interpretation and limitations of the mixing analysis

The analysis used in Section 4.2 uses the effective diffusivity k_{eff} , as defined in Eq. (2), as a proxy for the rate of density transformation from diffusive processes, including both physical and numerical mixing. As shown by several studies using this approach (Lee et al., 2002; Urakawa and Hasumi, 2014; Megann 2018; Megann and Storkey, 2021 and Megann et al., 2022), this provides a useful tool for assessing the sensitivity of numerical mixing to parameter and numerics changes in a given model configuration. Nevertheless, there are several aspects of the analysis where approximations are made and, although these do not substantially affect the conclusions of the present paper, they should be acknowledged as limitations of the analysis. Here we summarise the assumptions and approximations made.

A.1. The relationship between explicit mixing and numerical mixing

In this framework we assume implicitly that the difference between the effective diffusivity k_{eff} and the explicit diffusivity k_{exp} forms a useful proxy for numerical mixing, and furthermore that the relative degree of numerical mixing in any given regime may be expressed as the ratio $(k_{\text{eff}} - k_{\text{exp}})/k_{\text{exp}}$. Providing that the formulation of the explicit mixing is the same over the ensemble, and that the vertical density stratification does not vary significantly between members, this interpretation has been demonstrated to lead to a useful metric of mixing that shows sensitivities over a model ensemble that are consistent with those of other metrics such as temperature and salinity drifts. However, direct comparisons between the diagnosed effective diffusivity and the explicit diffusivity are less robust, for the following reason.

As mentioned in Section 3.2 of Megann and Storkey (2021), the expression for the effective diffusivity (Eq. (2)) is a ratio of the zonal integral of the meridional volume transport to that of the density stratification, and the assumption is made that the meridional velocity and the density stratification either have little variation, or both vary in a similar way, across each zonal section. This approximation is necessary for the derivation of a practical effective diffusivity, but the fact that the zonal integral of $\partial\rho/\partial z$ is made over the whole global domain, including very different regimes of mixing and stratification, in practice implies a degree of arbitrariness. This makes direct comparisons between k_{eff} and the explicit diffusivity k_{exp} unreliable; a more rigorous comparison might involve comparing the zonally integrated diffusive fluxes implied by the numerator of Eq. (2) with the diffusive fluxes evaluated from the model stratification and the explicit diffusivity. However, variations of the stratification between the ensemble members are

interests or personal relationships that could have appeared to influence the work reported in this paper.

Data availability

Data will be made available on request.

Acknowledgments

This paper is dedicated to the memory of Maria Luneva, without whom the work would have been far more challenging and less satisfying. The model configurations were set up under the project ‘‘Reducing numerical mixing resulting from applying tides explicitly in a global ocean model’’ (RENUMERATE) under the Copernicus Marine Environment Monitoring Service (CMEMS). CMEMS is implemented by Mercator Ocean International, in the framework of a delegation agreement with the European Union. It was also funded by the Natural Environment Research Council (NERC) under the Climate Linked Atlantic Sector Science (CLASS) marine research programme, as part of the Joint Marine Modelling Programme (JMMP), a strategic partnership between the Met Office and NERC. The model was integrated on the MONSooN system, a collaborative facility supplied under JMMP, while the analysis was carried out on the JASMIN platform, funded by NERC and maintained by the Centre for Environmental Data Analysis (CEDA). The author is grateful to Chris Wilson for providing the FES2014 data, to Adam Blaker, Jérôme Chanut and George Nurser for productive discussions, and to Adrian New for useful feedback on the manuscript. Finally, I am very grateful to the two anonymous reviewers and to the Editor, Remi Tailleux, for their helpful suggestions and probing questions, all of which have substantially improved the paper.

The source code for the modified GO8p0 version of the NEMO v4.0 configuration used in these integrations, along with the namelists and XML files, is archived at Zenodo: <https://zenodo.org/record/6652361>

The derived data used for the analysis presented here is archived at Zenodo: <https://zenodo.org/record/8276604>

very small, and all the comparisons we make in this paper, with the exception of Fig. 8(e), are between k_{eff} in different simulations. The latter figure panel shows the ratios of k_{eff} to k_{exp} for each simulation, and although these ratios are not reliable in an absolute sense, this figure is nevertheless informative, in the sense that it shows that the contribution of numerical mixing to the total mixing is most significant in the density range corresponding to intermediate and thermocline waters.

The definition of k_{eff} in Eq. (1) neglects density changes from surface buoyancy fluxes; in the analysis presented here, masking out the ventilated regions of density-latitude space according to the maximum surface density will substantially reduce the influence of surface fluxes, but solar shortwave radiation can penetrate deeper than the mixed layer base, especially in low-latitude regions. Although this is only likely to make small changes to the diagnosed effective diffusivity, the effect has not been quantified.

A.2. The contribution of isoneutral mixing to diapycnal density transformations

As noted by Lee et al., (2002), this framework ignores the convergence of the meridional diffusive flux, which may be significant in the eddy regimes in the Southern Ocean. These authors, however, point out that the error is of both signs in this region, and for that reason is likely to be less important on the large scale than that arising from neglecting cabbeling and thermobaricity, the contributions from both of the latter tending to be of the same sign over large regions. For these reasons it is not likely to be significant in the global means that we have presented here.

The fact that the isoneutral mixing scheme used in this configuration (Redi, 1982; Cox, 1987) mixes tracers along local neutral surfaces, whereas the mixing analysis is based on potential density, means that away from the 2000 dbar reference pressure there will be some leakage from isoneutral mixing into the diapycnal direction (e.g. Osborn, 1998; Hochet et al., 2019). Given that isoneutral mixing in the large scale tends to transport heat upwards (Griffies et al., 2015), this has the potential to produce apparently anti-diffusive transformations when projected into the isopycnal framework, and in any cases will contaminate the results from the analysis.

A.3. Contributions of thermobaricity and cabbeling to the density transformation rate

As noted by Lee et al., (2002), this analysis neglects thermobaricity and cabbeling, which result from the non-linear equation of state; both of these processes, as demonstrated by Klocker and McDougall (2010), lead to density fluxes in the Southern Ocean with signs corresponding to an overall tendency for densities to increase. Work to date based on the present mixing analysis has yielded negative values of the effective diffusivity (corresponding to up-gradient density fluxes) over regions in latitude and density space (mainly in the Southern Ocean, but also at subpolar latitudes in the North Atlantic) that are at least not inconsistent with the locations where the explicitly diagnosed density transformations from cabbeling and thermobaricity are largest, although no work to date has quantified these contributions to the effective diffusivity to confirm this. McDougall (1987) derives expressions for effective diffusivities from both processes, and it would be useful (though out of scope of this paper) to carry out a direct comparison of these in the present set of s_2 and latitude classes with the results presented here.

As shown by Hochet et al., (2019), the effect of thermobaricity on the potential density can be estimated by looking at the impact on effective diffusivity of including the effect of the isoneutral diffusivity in the diagnostics. This would be an interesting line of investigation, and indeed would be relatively straightforward to implement within the present framework, but crucially would not include the effects of cabbeling. For this reason, it is preferable to address this issue with a full analysis following the approach of McDougall (1987), as mentioned above.

A.4. Convergence of results with time averaging period

The effective diffusivity should ideally be evaluated from volume fluxes apportioned into potential density classes at each timestep during runtime, but for practical reasons all implementations of this method to date have used time-averaged model output fields: Lee et al., (2002), Megann (2018), Megann and Storkey (2021) and Megann et al., (2022) used a five-day averaging period as a practical compromise. High-frequency variation of the overturning strength of amplitude of over 100 Sv, associated with equatorial waves with periods of a few days, have been identified by Blaker et al., (2021), and it is possible that these waves, which are almost adiabatic in the real ocean, are aliased by the five-day sampling used here, and it is also likely that internal waves and internal tides, with periods between 12 and 24 h, are not accurately represented in the mean overturning streamfunction (see e.g. Yung and Holmes, 2023).

To investigate how closely the calculation based on five-day means converges to the solution that would be obtained during runtime, we evaluate the streamfunction from hourly output over three months at the start of 1996 for three of the ensemble members: *zstar_notide*; *zstar_tide*; and *ztilde_20_tide*. This frequency is short enough to satisfactorily resolve the external and internal tides, the internal gravity waves and the equatorial waves. We compare the contribution to k_{eff} of the divergence of the streamfunction in Eq. (2)

$$\kappa_{\text{eff}}^{(\text{div})} \equiv \int_{\rho_{\text{max}}}^{\rho} \frac{\partial \Psi(\Theta, \rho)}{\partial y} d\rho \bigg/ \int_{x_w}^{x_E} \frac{\partial \rho}{\partial z} dx \quad (3)$$

when evaluated from the five-day mean density and meridional velocity fields with that evaluated from hourly mean fields. We do not include here the contribution from the isopycnal volume drift $\frac{\partial}{\partial t} V(\Theta, \rho)$, since this is essentially independent of the sampling frequency.

Fig. 14(a), (b) and (c) show the differences between this term evaluated from hourly and 5-day means for *zstar_notide*, *zstar_tide* and *ztilde_20_tide*, averaged in each case over three months, with superposed contours of $\kappa_{\text{eff}}^{(\text{div})}$ itself. We note first of all that the errors are relatively small compared with $\kappa_{\text{eff}}^{(\text{div})}$ itself: the contours reach $45 \times 10^{-4} \text{ m}^2 \text{ s}^{-1}$, whereas the differences are generally smaller than about $\pm 3 \times 10^{-4} \text{ m}^2 \text{ s}^{-1}$. The main discrepancies are seen between 10°S and 10°N, where there is consistently a dipolar signal in the error field across the Equator, implying that the equatorial waves are being somewhat aliased by the 5-day sampling: this is confirmed by the observation (not shown here) that over the three months this dipolar feature changes sign from month to month, and the error is therefore likely to average to a rather smaller value over periods of a year or more. Smaller differences in all three simulations are seen between 40° and 50°N, which may be associated with NIGWs. It is notable that in *ztilde_20_tide* (Fig. 14(c)) significant differences of the same magnitude as those close to the Equator also occur in the Southern Ocean between 60°S and 30°S, but these again

alternate in sign from month to month. Fig. 14(d) shows the global mean of $\kappa_{eff}^{(div)}$ averaged over three months and over each individual month: this confirms that, while there is considerable variation vertically and from month to month, there appears to be convergence with time averaging on periods of three months towards a rather small mean value of less than $0.5 \times 10^{-5} \text{ m}^2 \text{ s}^{-1}$.

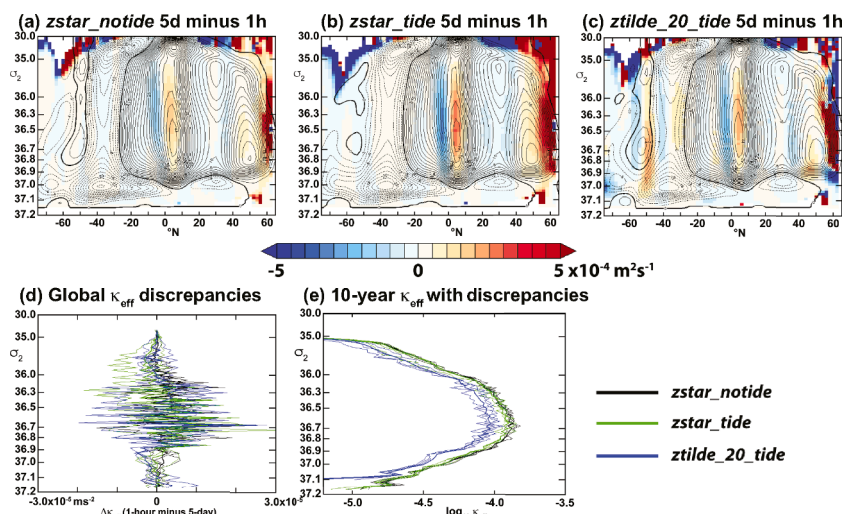


Fig. 14. Difference in zonal mean effective diffusivity (neglecting the isopycnal drift contribution) between that evaluated from hourly model output and that evaluated from 5-day means, averaged over three months, in (a) *zstar_notide*; (b) *zstar_tide*; and (c) *ztilde_20_tide*; the contours are of the effective diffusivity $\kappa_{eff}^{(div)}$ in each simulation. Panel (d) shows the global mean of $\kappa_{eff}^{(div)}$ averaged over three months (bold lines) and over individual months (thin lines), and Panel (e) shows the global mean effective diffusivity for these simulations (bold lines) evaluated from 5-day output, as in Fig. 8(c), with the three fine lines for each simulation displaced according to the global mean of the differences shown in 14(a), (b) and (c), the latter quantity evaluated for each of the three months.

The question remains whether the differences between five-day and hourly averaging when calculating k_{eff} constitute first-order errors, comparable with the differences in k_{eff} between different simulations. More specifically, does the error, when averaged over periods from a few months to the ten-year period used here, have a persistent systematic bias of similar or larger magnitude to the differences between ensemble members? Although hourly output was only generated for three months in each of the three integrations, it is informative for the latter question to compare the variation of the mean discrepancy in each month between the two sampling periods with the global mean effective diffusivities presented in Fig. 8. Fig. 14(e) shows the global mean k_{eff} curves for *zstar_notide*, *zstar_tide* and *ztilde_20_tide* as in Fig. 8(c), along with curves (fine lines) for each simulation displaced according to the global mean differences as shown in Fig. 14(d), the latter quantity evaluated for each of the three months. Although the displaced curves show significant variability around the ten-year means calculated from 5-day output, with magnitudes of the displacements that are comparable to the separation of the curves for different experiments, at most values of s_2 the effect of using 5-day output does not appear to give a systematic error, so is likely to average to a small mean value over the ten-year analysis period.

References

- Accad Y., and Pekeris C.L., 1978. Solution of the tidal equations for the M_2 and S_2 tides in the world oceans from a knowledge of the tidal potential alone. *Phil. Trans. Roy. Soc. Lon. Ser. A*, 290 (1978), pp. 235–266.
- Adcroft, A., Campin, J.M., 2004. Rescaled height coordinates for accurate representation of free-surface flows in ocean circulation models. *Ocean Model* 7, 269–284. <https://doi.org/10.1016/j.ocemod.2003.09.003> (Oxf).
- Adcroft, A., Anderson, W.G., Balaji, V., Blanton, C., Bushuk, M., Dufour, C.O., Dunne, J., Griffies, P., Hallberg, S.M., Harrison, R., Held, I.M., Jansen, M., John, J., Krasting, G., Langenhorst, J.P., Legg, A.R., S, Liang, McHugh, Z., Radhakrishnan, C., Reichl, A., Rosati, B.G., Samuels, A., Shao, B.L., Stouffer, A., Winton, M., Wittenberg, A.T., Xiang, B., Zadeh, N., Zhang, R., 2019. The GFDL global ocean and sea ice model OM4.0: model description and simulation features. *J. Adv. Model. Earth Syst.* 11 (10) <https://doi.org/10.1029/2019MS001726>.
- Arbic, B.K., Wallcraft, A.J., Metzger, E.J., 2010. Concurrent simulation of the eddy general circulation and tides in a global ocean model. *Ocean Model* 32, 175–187. <https://doi.org/10.1016/j.ocemod.2010.01.007>. (Oxf).
- Arbic, B.K., Richman, J.G., Shriver, J.F., Timko, P.G., Metzger, E.J., Wallcraft, A.J., 2012. Global modeling of internal tides within an eddy ocean general circulation model. *Oceanography* 25 (2), 20–29. <https://doi.org/10.5670/oceanog.2012.38>.
- Arbic, B.K., 2022. Incorporating tides and internal gravity waves within global ocean general circulation models: a review. *Prog. Oceanogr.* 206 (2022), 102824 <https://doi.org/10.1016/j.pocean.2022.102824>.
- Artioli, Y. et al., 2023. “Validated hindcast simulations 1980–2019 (NEMO-ERSEM & SEAPODYM)” Deliverable 6.1 from Horizons Europe Project Mission Atlantic <https://missionatlantic.eu>. Last accessed 18 January 2024.
- Barnier, B., Madec, G., Penduff, T., Molines, J.-M., Treguier, A.-M., Le Sommer, J., Beckmann, A., Biastoch, A., Böning, C., Dengg, J., Derval, C., Durand, E., Gulev, S., Remy, E., Talandier, C., Theetten, S., Maltrud, M., McClean, J., De Cuevas, B., 2006. Impact of partial steps and momentum advection schemes in a global ocean circulation model at eddy-permitting resolution. *Ocean Dynam.* 56, 543–567. <https://doi.org/10.1007/s10236-006-0082-1>.
- Barton, K.N., Pal, N., Brus, S.R., Petersen, M.R., Arbic, B.K., Engwirda, D., et al., 2022. Global barotropic tide modeling using inline self-attraction and loading in MPAS-Ocean. *JAMES* 14, e2022MS003207. <https://doi.org/10.1029/2022MS003207>.
- Blaker, A.T., Hirschi, J.J.M, Bell, M.J., Bokota, A., 2021. Wind-driven oscillations in the meridional overturning circulation near the equator. Part I: numerical models. *J. Phys. Oceanogr.* 51 (3), 645–661. <https://doi.org/10.1175/JPO-D-19-0296.1>.
- Bleck, R., 2002. An oceanic general circulation model framed in hybrid isopycnal-cartesian coordinates. *Ocean Modell.* 5 55–88.
- Bryan, F., 1987. Parameter sensitivity of primitive equation ocean general circulation models. *J. Phys. Oceanogr.* 17, 970–985.
- Cimoli, L., Mashayek, A., Johnson, H.L., Marshall, D.P., Naveira Garabato, A.C., Whalen, C.B., et al., 2023. Significance of diapycnal mixing within the Atlantic meridional overturning circulation. *AGU Adv.* 4, e2022AV000800.
- Cox, M.D., 1987. Isopycnal diffusion in a z-coordinate ocean model. *Ocean Model* 74, 1–5. (Oxf).
- De Lavergne, C., Madec, G., le Sommer, J., Nurser, A.J.G., Garabato, A.C.N., 2016. On the consumption of antarctic bottom water in the abyssal ocean. *J. Phys. Oceanogr.* 46, 635–661.
- De Lavergne, C., Vic, C., Madec, G., Roquet, F., Waterhouse, A.F., Whalen, C.B., et al., 2020. A parameterization of local and remote tidal mixing. *J. Adv. Model. Earth Syst.* 12, e2020MS002065 <https://doi.org/10.1029/2020MS002065>.
- Egbert, G.D., Ray, R.D., 2001. Estimates of M_2 tidal energy dissipation from TOPEX/Poseidon altimeter data. *J. Geophys. Res.* 106, 22475–22502.
- Garrett, C.J., Munk, W., 1975. Space-time scales of internal waves: a progress report. *J. Geophys. Res.* 80, 291–297.
- Gaspar, P., Grégoris, Y., Lefevre, J.-M., 1990. A simple eddy kinetic energy model for simulations of the oceanic vertical mixing: tests at Station Papa and long-term upper ocean study site. *J. Geophys. Res.* 95, 16179–16193. <https://doi.org/10.1029/JC095iC09p16179>, 1990.
- Gibson, A.H., Hogg, A.M., Kiss, A.E., Shakespeare, C.J., Adcroft, A., 2017. Attribution of horizontal and vertical contributions to spurious mixing in an Arbitrary Lagrangian-Eulerian ocean model. *Ocean Model* 119, 45–56. <https://doi.org/10.1016/j.ocemod.2017.09.008>. (Oxf).

- Good, S.A., Martin, M.J., Rayner, N.A., 2013. EN4: quality controlled ocean temperature and salinity profiles and monthly objective analyses with uncertainty estimates. *JGR Oceans* 118, 6704–6716.
- Griffies, S. M., and W. Hallberg, R., Biharmonic friction with a Smagorinsky-like viscosity for use in large-scale eddy-permitting ocean models. *Mon. Wea. Rev.*, 128 (8), 2935–2946, 2000.
- Griffies, S., Pacanowski, R.C., Hallberg, R.W., 2000. Spurious diapycnal mixing associated with advection in a z-coordinate ocean model. *Mon. Weather Rev.* 128 (3), 538–564.
- Griffies, S.M., Winton, M., Anderson, W.G., Benson, R., Delworth, T.L., Dufour, C.O., Dunne, J.P., Goddard, P., Morrison, Adele K, Wittenberg, Andrew T, Yin, Jianjun, Zhang, Rong, 2015. Impacts on ocean heat from transient mesoscale eddies in a hierarchy of climate models. *J. Climate* 28, 952–977. <https://doi.org/10.1175/JCLI-D-14-00353.1>.
- Hochet, A., Tailleux, R., Ferreira, D., Kuhlbrodt, T., 2019. Isonutral control of effective diapycnal mixing in numerical ocean models with neutral rotated diffusion tensors. *Ocean Sci.* 15, 21–32.
- Hogg, N.G., Biscaye, P., Gardner, W., Schmitz, W.J., 1982. On the transport and modification of Antarctic Bottom water in the vema channel. *J. Mar. Res.* 40 (Suppl), 231–263.
- Holloway, G., Proshutinsky, A., 2007. Role of tides in arctic ocean/ice climate. *J. Geophys. Res.* 112 <https://doi.org/10.1029/2006JC003643>.
- Holmes, R.M., Zika, J.D., Griffies, S.M., Hogg, A.M., Kiss, A.E., England, M.H., 2021. The geography of numerical mixing in a suite of global ocean models. *J. Adv. Model. Earth Syst.* 13, e2020MS002333 <https://doi.org/10.1029/2020MS002333>.
- Hyder, P., Edwards, J., Allan, R.P., et al., 2018. Critical Southern Ocean climate model biases traced to atmospheric model cloud errors. *Nat. Commun.* 9, 3625. <https://doi.org/10.1038/s41467-018-05634-2>.
- Jayne, S.R., 2009. The impact of abyssal mixing parameterizations in an ocean general circulation model. *J. Phys. Oceanogr.* 39, 1756–1775. <https://doi.org/10.1175/2009JPO4085.1>.
- Johnson, G.C., Bryden, H.L., 1989. On the size of the antarctic circumpolar current. *Deep Sea Res. A* 36, 39–53. [https://doi.org/10.1016/0198-0149\(89\)90017-4](https://doi.org/10.1016/0198-0149(89)90017-4).
- Jourdain, N., Molines, J.-M., Le Sommer, J., Mathiot, P., Chanut, J., deLavergne, C., Madec, G., 2019. Simulating or prescribing the influence of tides on the Amundsen Sea ice shelves. *Ocean Model* 133, 44–55. <https://doi.org/10.1016/j.ocemod.2018.11.001> (Oxf).
- Katavouta, A., Polton, J. A., Harle, J.D., Holt, J.T., 2022. Effect of tides on the Indonesian seas circulation and their role on the volume, heat and salt transports of the Indonesian throughflow. *J. Geophys. Res.* (8), 127. <https://doi.org/10.1029/2022JC018524> (Oceans).
- Kloeker, A., McDougall, T.J., 2010. Influence of the nonlinear equation of state on global estimates of diapycnal advection and diffusion. *J. Phys. Oceanogr.* 40, 1690–1709.
- Koch-Larrouy, A., Madec, G., Blanke, B., Molcard, R., 2008. Water mass transformation along the Indonesian throughflow in an OGCM. *Ocean Dyn.* 58 <https://doi.org/10.1007/s10236-008-0155-4>.
- Large, W.G., Yeager, S.G., 2009. The global climatology of an interannually varying air-sea flux data set. *Clim. Dynam.* 33, 341–364. <https://doi.org/10.1007/s00382-008-0441-3>, 2009.
- Leclair, M., Madec, G., 2011. z~–Coordinate, an Arbitrary Lagrangian–Eulerian coordinate separating high and low frequency motions. *Ocean Model* 37, 139–152 (Oxf).
- Lee, M.-M., Coward, A.C., Nurser, A.G., 2002. Spurious diapycnal mixing of deep waters in an eddy-permitting global ocean model. *J. Phys. Oceanogr.* 32, 1522–1535.
- Levier, B., Tréguier, A.M., Madec, G., Garnier, V., 2007. : free surface and variable volume in the nemo code. *TechRep.* , MERSEA IP report WP09-CNRS-STR-03-1A, 47pp. <https://zenodo.org/record/3244182/export/hx#.Y1JaqS8w1R4>.
- Luneva, M.V., Aksenov, Y.K., Harle, J.D., Holt, J.T., 2015. The effects of tides on the water mass mixing and sea ice in the Arctic Ocean. *JGR Oceans* 120, 6669–6699.
- Lyard, F.H., Allain, D.J., Cancet, M., Carrère, L., Picot, L., 2021. FES2014 global ocean tide atlas: design and performance. *Ocean Sci.* 17, 615–649. <https://doi.org/10.5194/os-17-615-2021>.
- Madec, G., Bourdallé-Badie, R., Bouttier, P.A., Bricaud, C., Bruciaferri, D., Calvert, D., Chanut, J., E, Clementi, Coward, C., Delrosso, D., Ethé, C., Flavoni, S., Graham, T., Harle, J., Iovino, D., Lea, D., Lévy, C., Lovato, T., Martin, N., Masson, S., Mocarero, S., Paul, J., Rousset, C., Storkey, D., Storto, A., Vancoppenolle, M., 2019. NEMO Ocean Engine. <https://doi.org/10.5281/zenodo.1464816>.
- Marzocchi, A., Hirschi, J.J.-M., Holliday, N.P., Cunningham, S.A., Blaker, A.T., Coward, A. C., 2015. The North Atlantic subpolar circulation in an eddy-resolving global ocean model. *J. Mar. Syst.* 142, 126–143. <https://doi.org/10.1016/j.jmarsys.2014.10.007>.
- McDougall, T.J., 1987. Thermobaricity, cabelling and water-mass conversion. *J. Geophys. Res.* 92 (C5), 5448–5464.
- Megann, A., Storkey, D., 2021. Exploring viscosity space in an eddy-permitting global ocean model: is viscosity a useful control for numerical mixing? *JAMES* 13. <https://doi.org/10.1029/2020MS002263>.
- Megann, A., Chanut, J., Storkey, D., 2022. Assessment of the z~ time-filtered Arbitrary Lagrangian-Eulerian coordinate in a global eddy-permitting ocean model. *JAMES* 14, e2022MS003056. <https://doi.org/10.1029/2022MS003056>.
- Megann, A., 2018. Estimating the numerical diapycnal mixing in an eddy-permitting ocean model. *Ocean Model* 121, 19–33. <https://doi.org/10.1016/j.ocemod.2017.11.001> (Oxf).
- Munk, W., Wunsch, C., 1998. Abyssal recipes II: energetics of tidal and wind mixing. *Deep Sea Res.* 45, 1977–2010. [https://doi.org/10.1016/S0967-0637\(98\)00070-3](https://doi.org/10.1016/S0967-0637(98)00070-3).
- Osborn, T.J., 1998. The vertical component of epineutral diffusion and the diapycnal component of horizontal diffusion. *J. Phys. Oceanogr.* 28, 485–494.
- Petersen, M.R., Jacobsen, D.W., Ringler, T.D., Hecht, M.W., Maltrud, M.E., 2015. Evaluation of the arbitrary Lagrangian–Eulerian vertical coordinate method in the MPAS-Ocean model. *Ocean Model* 86, 93–113. (Oxf).
- Pringle, W.J., Wirasaet, D., Roberts, K.J., Westerink, J.J., 2021. Global storm tide modelling with ADCIRC v55: Unstructured mesh design and performance. *Geosci. Model Dev.* 14 (2), 1125–1145. <https://doi.org/10.5194/gmd-14-1125-2021>.
- Ray, R.D., Mitchum, G.T., 1997. Surface manifestation of internal tides in the deep ocean: observations from altimetry and island gauges. *Prog. Oceanogr.* 40, 35–162. [https://doi.org/10.1016/S0079-6611\(97\)00025-6](https://doi.org/10.1016/S0079-6611(97)00025-6).
- Ray, R.D., Zaron, E.D., 2016. M2 Internal tides and their observed wavenumber spectra from satellite altimetry. *J. Phys. Oceanogr.* 46, 3–22. <https://doi.org/10.1175/JPO-D-15-0065.1>.
- Rayner, N.A., Parker, D.E., Horton, E.B., Folland, C.K., Alexander, L.V., Rowell, D.P., Kent, E.C., Kaplan, A., 2003. Global analyses of sea surface temperature, sea ice, and night marine air temperature since the late nineteenth century. *J. Geophys. Res.* Atmos. 108, 4407. <https://doi.org/10.1029/2002JD002670>.
- Redi, M.H., 1982. Oceanic isopycnal mixing by coordinate rotation. *J. Phys. Oceanogr.* 12, 1154–1158.
- Saenko, O.A., Merryfield, W.J., 2005. On the effect of topographically enhanced mixing on the global ocean circulation. *J. Phys. Oceanogr.* 35, 826–834.
- Sakai, A., Senjyu, T., Matsuno, T., Tsutsumi, E., Endoh, T., 2021. Internal waves with high vertical wavenumber structure generated by diurnal tidal flow over the eastern ridge of Luzon Strait. *J. Oceanogr.* 77 (2021), 703–718. <https://doi.org/10.1007/s10872-021-00615-4>.
- Sasaki, H., Kida, S., Furue, R., Nonaka, M., Matsumoto, Y., 2018. An Increase of the Indonesian throughflow by internal tidal mixing in a high-resolution quasi-global ocean simulation. *Geophys. Res. Lett.* 45, 8416–8424. <https://doi.org/10.1029/2018GL078040>.
- Scott, J.R., Marotzke, J., 2002. Diapycnal stirring and meridional overturning circulation: does it matter where the mixing occurs? *J. Phys. Oceanogr.* 32, 3578–3595.
- Sharples, J., Tweedle, J.F., Green, J.A.M., Palmer, M.R., Kim, Y.N., Hickman, A.E., Holligan, P.M., Moore, C.M., Rippeth, T.P., Simpson, J.H., Krivtsov, V., 2007. Spring-neap modulation of internal tide mixing and vertical nitrate fluxes at a shelf edge in summer. *Limnol. Oceanogr.* 52, 1735–1747.
- Simmons, H.L., Jayne, S.R., St. Laurent, L.C., Weaver, A.J., 2004. Tidally driven mixing in a numerical model of the ocean general circulation. *Ocean Model* 6, 245–263. (Oxf).
- Song, P., Sidorenko, D., Scholz, P., Thomas, M., Lohmann, G., 2023. The tidal effects in the finite-volume sea ice–ocean model (FESOM2.1): a comparison between parameterised tidal mixing and explicit tidal forcing. *Geosci. Model Dev.* 16, 383–405. <https://doi.org/10.5194/gmd-16-383-2023>.
- Sprintall, J., Wijffels, S., Molcard, R., Jaya, I., 2009. Direct estimates of the Indonesian throughflow entering the Indian ocean. *J. Geophys. Res.* 114, C07001. <https://doi.org/10.1029/2008JC005257>.
- St Laurent, L.C., Simmons, H.L., Jayne, S.R., 2002. Estimating tidally driven mixing in the deep ocean. *Geophys. Res. Lett.* 29, 2106. <https://doi.org/10.1029/2002GL015633>.
- St. Laurent, L.C., Garrett, C., 2002. The role of internal tides in mixing the deep ocean. *J. Phys. Oceanogr.* 32, 2882–2899. [https://doi.org/10.1175/1520-0485\(2002\)032<2882:TROI.2.0.CO;2](https://doi.org/10.1175/1520-0485(2002)032<2882:TROI.2.0.CO;2).
- Storkey, D., Blaker, A.T., Mathiot, P., Megann, A., Aksenov, Y., Blockley, E.W., Calvert, D., Graham, T., Hewitt, H.T., Hyder, P., Kuhlbrodt, T., Rae, J.G.L., Sinha, B., 2018. UK global ocean G06 and G07: a traceable hierarchy of model resolutions. *Geosci. Model Dev.* 11, 3187–3213. <https://doi.org/10.5194/gmd-11-3187-2018>.
- Tuerena, R.E., Williams, R.G., Mahaffey, C., Vic, C., Green, J.A.M., Naveira-Garabato, A., Forryan, A., Sharples, J., 2019. Internal tides drive nutrient fluxes into the deep chlorophyll maximum over mid-ocean ridges. *Glob. Biogeochem. Cycles* 33, 995–1009.
- Urakawa, L.S., Hasumi, H., 2014. Effect of numerical diffusion on the water mass transformation in eddy-resolving models. *Ocean Model* 74, 22–35. <https://doi.org/10.1016/j.ocemod.2013.11.003>. (Oxf).
- Vic, C., Naveira Garabato, A.C., Green, J.A.M., Waterhouse, A.F., Zhao, Z., Melet, A., de Lavergne, C., Buijsman, M.C., Stephenson, G.R., 2019. Deep-ocean mixing driven by small-scale internal tides. *Nat. Commun.* 10, 2099. <https://doi.org/10.1038/s41467-019-10149-5>.
- Waterhouse, A.F., MacKinnon, J.A., Nash, J.D., Alford, M.H., Kunze, E., Simmons, H.L., Polzin, K.L., St Laurent, L.C., Sun, O.M., Pinkel, R., Talley, L.D., Whalen, C.B., Huussen, T.N., Carter, G.S., Fer, I., Waterman, S., Naveira Garabato, A.C., Sanford, T.B., Lee, C.M., 2014. Global patterns of diapycnal mixing from measurements of the turbulent dissipation rate. *J. Phys. Oceanogr.* 44 (7), 1854–1872.
- Webb, D.J., Sugimoto, N., 2001. Int. *Geophys.* 77, 205–214. [https://doi.org/10.1016/S0074-6142\(01\)80120-0](https://doi.org/10.1016/S0074-6142(01)80120-0).
- Whitehead, J.A., Wang, W., 2008. A laboratory model of vertical ocean circulation driven by mixing. *J. Phys. Oceanogr.* 38, 1091–1106.
- Wunsch, C., Ferrari, R., 2004. Vertical mixing, energy, and the general circulation of the oceans. *Annu. Rev. Fluid Mech.* 36, 281–314. <https://doi.org/10.1146/annurev.fluid.36.050802.122121>.
- Yung, C.K., Holmes, R.M., 2023. On the contribution of transient diabatic processes to ocean heat transport and temperature variability. *J. Phys. Oceanogr.* 53, 2933–2951. <https://doi.org/10.1175/JPO-D-23-0046.1>.
- Zalesak, S.T., 1979. Fully multidimensional flux corrected transport algorithms for fluids. *J. Comput. Phys.* 31, 335–362. <https://doi.org/10.5670/oceanog.2012.40>.

Zhang, J., Rothrock, D.A., 2003. Modeling global sea ice with a thickness and enthalpy distribution model in generalized curvilinear coordinates. *Mon. Weather Rev.* 131, 845–861. [https://doi.org/10.1175/1520-0493\(2003\)131h0845:MGSIWai2.0.CO;2](https://doi.org/10.1175/1520-0493(2003)131h0845:MGSIWai2.0.CO;2).

Zhao, Z., Alford, M.H., Girton, J.B., Rainville, L., Simmons, H.L., 2016. Global observations of open-ocean mode-1 M_2 internal tides. *J. Phys. Oceanogr.* 46, 1657–1684. <https://doi.org/10.1175/JPO-D-15-0105.1>.

Zhao, Z., 2018. The global Mode-2 M_2 internal Tide. *J. Geophys. Res.* 123, 7725–7746. <https://doi.org/10.1029/2018JC014475>.